Commun. Comput. Phys.
doi: 10.4208/cicp.OA-2024-0088

Vol. **37**, No. 1, pp. 193-219
January 2025

Application of MUSIC Algorithm for Object Localization Without Diagonal Elements of Multi-Static Response Matrix

Won-Kwang Park*

Department of Information Security, Cryptology, and Mathematics, Kookmin University, Seoul, 02707, Korea

Received 15 April 2024; Accepted (in revised version) 23 August 2024

Abstract. Generally, to apply the MUltiple SIgnal Classification (MUSIC) algorithm for the rapid imaging of small objects, complete elements of the multi-static response (MSR) matrix must be collected. However, in some real-world applications in microwave imaging, diagonal elements of the MSR matrix are unknown. Nevertheless, it is possible to obtain imaging results using a traditional approach but theoretical reason of the applicability has not been investigated yet. In this paper, we consider the application of MUSIC for a fast identification of small objects from collected MSR matrix in both transverse magnetic (TM) and transverse electric (TE) polarizations. In order to examine the applicability, fundamental limitation, and various properties of MUSIC, we establish mathematical structure of the three imaging functions and explore that the main factors of the imaging functions are Bessel function of order zero, one, and two. The established structures demonstrate why the existence and location of small objects can be retrieved via MUSIC without the diagonal elements of the MSR matrix. Results of numerical simulations with noise-corrupted synthetic data are also provided to support the identified structures.

AMS subject classifications: 78A46

Key words: MUltiple SIgnal Classification (MUSIC), multi-static response (MSR) matrix, Bessel functions, numerical simulations.

1 Introduction

Time-harmonic inverse scattering problems for the retrieval of a two-dimensional small objects in transverse magnetic (TM) polarization (or permittivity contrast case) and transverse electric (TE) polarization (or permeability contrast case) have been considered in

*Corresponding author. *Email address:* parkwk@kookmin.ac.kr (W.-K. Park)

 ©2025 Global-Science Press

various researches [3,9,12,15,19,35]. The principle of retrieving unknown targets is based on the Newton iteration method (i.e., determining the shape of the objects), which minimizes the discrepancy function between the measured far-field patterns in the presence of true and man-made targets. Various techniques for reconstructing the shape of targets have also been developed, including the Newton or Gauss-Newton methods [33, 54], level-set strategy [21,48], bifocusing method [27,51], factorization method [31,34], potential drop method [25], inverse Fourier transform [2], migration techniques [6, 42], topological derivative [4, 37], direct sampling method [26, 41], and linear sampling method [16,32].

The MUltiple SIgnal Classification (MUSIC) algorithm has been successfully used for imaging arbitrary shaped targets. For example, identification of two- and three-dimensional small targets [8,17], retrieving small targets completely embedded in a half-space [7, 24], detecting internal corrosion [10], damage diagnosis on complex aircraft structures [13], reconstruction of thin objects [38], perfectly conducting cracks [11], and extended targets [5], radar imaging [36], and biomedical imaging [50]. Throughout various researches, it has been confirmed that MUSIC is a fast, stable, and effective imaging technique. Furthermore, MUSIC can be extended in a straightforward fashion to the case of multiple non-overlapping objects. Recently, by establishing relationships with Bessel functions of integer order, various intrinsic properties of MUSIC in full- and limited-view, and limited-aperture inverse scattering problems have been revealed [1, 28, 30, 44, 46].

In several studies, the MUSIC algorithm has been applied when one can use the complete elements of a multi-static response (MSR) matrix whose elements are measured scattered field or far-field pattern. However, under certain configurations, the diagonal elements of an MSR matrix cannot be handled. For example, it is very hard to simultaneously transmit and receive the signal in microwave imaging (see [14, 43, 52] for instance) so that the assumption that all elements of the MSR matrix are available cannot be used. This is the reason of the development of bistatic imaging technique to overcome intrinsic limitation of monostatic imaging, refer to [18, 20, 29]. Fortunately, the shape of objects can still be obtained via MUSIC without diagonal elements of MSR matrix. This fact can be examined through various numerical simulation; however, the theoretical reasons for its applicability have not been investigated. This provides a stimulus for analyzing the MUSIC algorithm without the diagonal elements of an MSR matrix.

In this study, we consider the MUSIC algorithm for imaging two-dimensional small object in TM and TE polarization from MSR matrix when the diagonal elements cannot be handled. In order to show the feasibility, we carefully investigate the mathematical structure of a MUSIC-type imaging function by identifying a connection with the Bessel function of integer order of the first kind. This is based on the asymptotic expansion formula in the presence of small object in TM and TE polarizations, refer to [9]. The investigated structure explains why the location of objects can be obtained via MUSIC in both TM and TE polarizations, and it reveals the undiscovered properties of MUSIC. In order to support the theoretical results, simulation results with synthetic data polluted by random noise are exhibited.

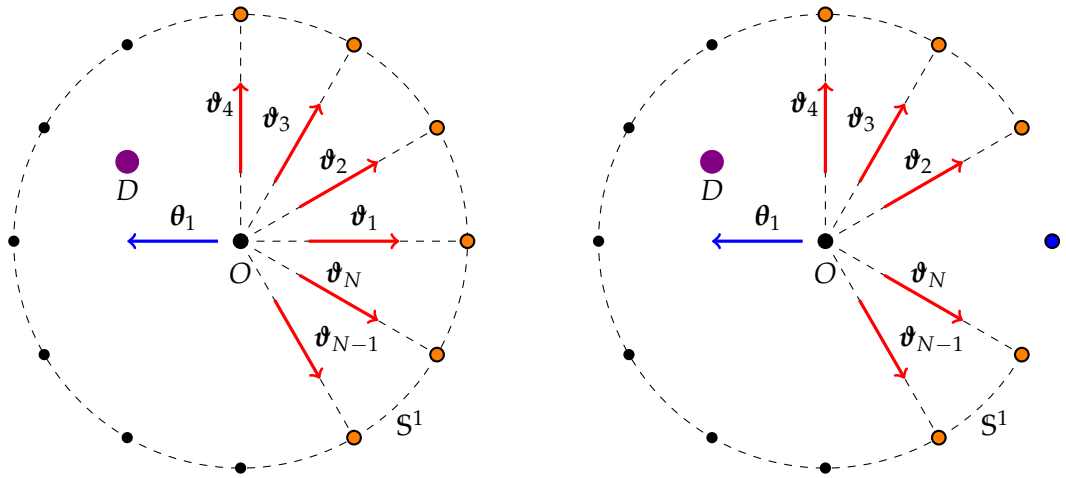

Figure 1: Illustrations of traditional (left) and current (right) simulation configurations corresponding the incident direction θ_1.

The paper is organized as follows. In Section 2, we describe the two-dimensional direct scattering problem and introduce the far-field pattern in the presence of small objects. In Section 3, we introduce the traditional MUSIC algorithm. In Section 4, we introduce the MUSIC algorithm, analyze the structure of the imaging functions from the MSR matrix without diagonal elements, and discuss their properties. In Section 5, we present the results of numerical simulations to support the analyzed structure of MUSIC. Finally, in Section 6, we present a short conclusion including future work.

2 Direct scattering problem and far-field pattern

In this section, we introduce two-dimensional electromagnetic scattering in the presence of small object in TM and TE polarizations. For a detailed description, we recommend [9, 49, 53] for a more detailed discussion. We assume that there exists a circle-like small object D with radius α and center $\mathbf{z}$, and every materials are characterized by the value of dielectric permittivity and magnetic permeability at the given angular frequency $\omega=2\pi f$. Here, f denotes the ordinary frequency measured in `hertz`.

Let ε_a and μ_a denote the value of dielectric permittivity and magnetic permeability of D, respectively, and we denote ε_b and μ_b be those of $\mathbb{R}^2\setminus\overline{D}$. With this, the following piecewise constants of dielectric permittivity and magnetic permeability can be introduced;

$$\varepsilon(\mathbf{x})=\begin{cases}\varepsilon_a & \text{for } \mathbf{x}\in D,\\ \varepsilon_b & \text{for } \mathbf{x}\in\mathbb{R}^2\setminus\overline{D},\end{cases}\quad\text{and}\quad \mu(\mathbf{x})=\begin{cases}\mu_a & \text{for } \mathbf{x}\in D,\\ \mu_b & \text{for } \mathbf{x}\in\mathbb{R}^2\setminus\overline{D}.\end{cases}$$

With this, we denote k_b be the background wavenumber that satisfies $k_b^2=\omega^2\varepsilon_b\mu_b$.

In this paper, we consider the illumination of plane waves with the direction of propagation $\boldsymbol{\theta}\in\mathbb{S}^1$:

$$u_{\text{inc}}(\mathbf{x},\boldsymbol{\theta})=e^{ik_b\boldsymbol{\theta}\cdot\mathbf{x}},$$

where $\mathbb{S}^1$ is a two-dimensional unit circle centered at the origin. Then, the scattering of $u_{\text{inc}}(\mathbf{x},\boldsymbol{\theta})$ by D leads to the following direct scattering problem for the Helmholtz equation; let $u(\mathbf{x},\boldsymbol{\theta})$ be the time-harmonic total field; then, it satisfies

$$\nabla\cdot\left(\frac{1}{\mu(\mathbf{x})}\nabla u(\mathbf{x},\boldsymbol{\theta})\right)+\omega^2\varepsilon(\mathbf{x})u(\mathbf{x},\boldsymbol{\theta})=0 \quad \text{for } \mathbf{x}\in\mathbb{R}^2$$

with transmission conditions at the boundaries of D. We denote $u_{\text{scat}}(\mathbf{x},\boldsymbol{\theta})=u(\mathbf{x},\boldsymbol{\theta})-u_{\text{inc}}(\mathbf{x},\boldsymbol{\theta})$ as the scattered field, which is required to satisfy the Sommerfeld radiation condition

$$\lim_{|\mathbf{x}|\to\infty}|\mathbf{x}|^{1/2}\left(\frac{\partial u_{\text{scat}}(\mathbf{x},\boldsymbol{\theta})}{\partial|\mathbf{x}|}-ik_b u_{\text{scat}}(\mathbf{x},\boldsymbol{\theta})\right)=0$$

uniformly in all directions $\boldsymbol{\vartheta}=\mathbf{x}/|\mathbf{x}|\in\mathbb{S}^1$.

Let $u_\infty(\boldsymbol{\vartheta},\boldsymbol{\theta})$ be the far-field pattern of the scattered field $u_{\text{scat}}(\mathbf{x},\boldsymbol{\theta})$ with observation direction $\boldsymbol{\vartheta}\in\mathbb{S}^1$ that satisfies

$$u_{\text{scat}}(\mathbf{x},\boldsymbol{\theta})=\frac{e^{ik_b|\mathbf{x}|}}{\sqrt{|\mathbf{x}|}}u_\infty(\boldsymbol{\vartheta},\boldsymbol{\theta})+o\left(\frac{1}{\sqrt{|\mathbf{x}|}}\right) \quad \text{uniformly in all directions} \quad \boldsymbol{\vartheta}=\frac{\mathbf{x}}{|\mathbf{x}|}, \quad |\mathbf{x}|\longrightarrow\infty.$$

Then, by virtue of [9], the far-field pattern $u_\infty(\boldsymbol{\vartheta},\boldsymbol{\theta})$ can be represented as an asymptotic expansion formula, which plays a key role in designing the MUSIC algorithm.

Lemma 2.1 (Asymptotic Expansion Formula)**.** *For sufficiently large ω, $u_\infty(\boldsymbol{\vartheta},\boldsymbol{\theta})$ can be represented as*

$$u_\infty(\boldsymbol{\vartheta},\boldsymbol{\theta})=\alpha^2\pi\frac{k_b^2(1+i)}{4\sqrt{k_b\pi}}\left(\frac{\varepsilon_a-\varepsilon_b}{\sqrt{\varepsilon_b\mu_b}}-\frac{2\mu_b}{\mu_a+\mu_b}(\boldsymbol{\vartheta}\cdot\boldsymbol{\theta})\right)e^{-ik_b(\boldsymbol{\vartheta}-\boldsymbol{\theta})\cdot\mathbf{z}}+o(\alpha^2). \tag{2.1}$$

3 Traditional MUSIC algorithm

In this section, we introduce the traditional MUSIC algorithm for imaging D in dielectric permittivity (or TM polarization) and magnetic permeability (or TE polarization) cases. For the sake of simplicity, suppose that we have $N-$different number of incident and observation directions $\boldsymbol{\theta}_n$ and $\boldsymbol{\vartheta}_m$, respectively, for $n,m=1,2,\cdots,N$, and that the incident and observation directions are the same (i.e., $\boldsymbol{\vartheta}_n=-\boldsymbol{\theta}_n$). In this paper, we consider the full-view inverse problem. Therefore, we assume that $\boldsymbol{\theta}_n$ is uniformly distributed in $\mathbb{S}^1$ such that

$$\boldsymbol{\theta}_n=\left[\cos\frac{2\pi n}{N},\sin\frac{2\pi n}{N}\right]. \tag{3.1}$$

Traditionally, the following MSR matrix is used in the MUSIC algorithm:

$$\mathbb{M}=\begin{bmatrix} u_\infty(\boldsymbol{\vartheta}_1,\boldsymbol{\theta}_1) & u_\infty(\boldsymbol{\vartheta}_1,\boldsymbol{\theta}_2) & \cdots & u_\infty(\boldsymbol{\vartheta}_1,\boldsymbol{\theta}_{N-1}) & u_\infty(\boldsymbol{\vartheta}_1,\boldsymbol{\theta}_N) \\ u_\infty(\boldsymbol{\vartheta}_2,\boldsymbol{\theta}_1) & u_\infty(\boldsymbol{\vartheta}_2,\boldsymbol{\theta}_2) & \cdots & u_\infty(\boldsymbol{\vartheta}_2,\boldsymbol{\theta}_{N-1}) & u_\infty(\boldsymbol{\vartheta}_2,\boldsymbol{\theta}_N) \\ \vdots & \vdots & \ddots & \vdots & \vdots \\ u_\infty(\boldsymbol{\vartheta}_N,\boldsymbol{\theta}_1) & u_\infty(\boldsymbol{\vartheta}_N,\boldsymbol{\theta}_2) & \cdots & u_\infty(\boldsymbol{\vartheta}_N,\boldsymbol{\theta}_{N-1}) & u_\infty(\boldsymbol{\vartheta}_N,\boldsymbol{\theta}_N) \end{bmatrix}.$$

First, let us assume that $\varepsilon(\mathbf{x})\neq\varepsilon_{\mathrm{b}}$ and $\mu(\mathbf{x})=\mu_{\mathrm{b}}$. Based on (2.1), since $u_\infty(\boldsymbol{\vartheta}_m,\boldsymbol{\theta}_n)$ can be approximated as

$$u_\infty(\boldsymbol{\vartheta}_m,\boldsymbol{\theta}_n)\approx\alpha^2\pi\frac{k_{\mathrm{b}}^2(1+i)}{4\sqrt{k_{\mathrm{b}}\pi}}\left(\frac{\varepsilon_{\mathrm{a}}-\varepsilon_{\mathrm{b}}}{\sqrt{\varepsilon_{\mathrm{b}}\mu_{\mathrm{b}}}}\right)e^{-ik_{\mathrm{b}}(\boldsymbol{\vartheta}_m-\boldsymbol{\theta}_n)\cdot\mathbf{z}},$$

MSR matrix $\mathbb{M}$ can be written as

$$\mathbb{M}\approx\alpha^2\pi\frac{k_{\mathrm{b}}^2(1+i)}{4\sqrt{k_{\mathrm{b}}\pi}}\left(\frac{\varepsilon_{\mathrm{a}}-\varepsilon_{\mathrm{b}}}{\sqrt{\varepsilon_{\mathrm{b}}\mu_{\mathrm{b}}}}\right)\mathbb{E}(\mathbf{z})^T\mathbb{E}(\mathbf{z}), \tag{3.2}$$

where

$$\mathbb{E}(\mathbf{z})=\left[e^{-ik_{\mathrm{b}}\boldsymbol{\vartheta}_1\cdot\mathbf{z}},e^{-ik_{\mathrm{b}}\boldsymbol{\vartheta}_2\cdot\mathbf{z}},\cdots,e^{-ik_{\mathrm{b}}\boldsymbol{\vartheta}_N\cdot\mathbf{z}}\right]\Big|_{\boldsymbol{\vartheta}_m=-\boldsymbol{\theta}_m}=\left[e^{ik_{\mathrm{b}}\boldsymbol{\theta}_1\cdot\mathbf{z}},e^{ik_{\mathrm{b}}\boldsymbol{\theta}_2\cdot\mathbf{z}},\cdots,e^{ik_{\mathrm{b}}\boldsymbol{\theta}_N\cdot\mathbf{z}}\right]. \tag{3.3}$$

Based on the factorization of the MSR matrix, the range of $\mathbb{M}$ is determined by the span of $\mathbb{E}(\mathbf{z})$ corresponding to D; that is, we can define a signal subspace using a set of singular vectors corresponding to the nonzero singular values of $\mathbb{M}$.

Now, to introduce the imaging function of MUSIC, let us perform the singular value decomposition (SVD) of the MSR matrix $\mathbb{M}$:

$$\mathbb{M}=\sum_{n=1}^{N}\sigma_n\mathbf{E}_n\mathbf{F}_n^*\approx\sigma_1\mathbf{E}_1\mathbf{F}_1^*,$$

where superscript $*$ is the mark of Hermitian, $\mathbf{E}_n$ and $\mathbf{F}_n\in\mathbb{C}^{N\times1}$ are respectively the left- and right-singular vectors of $\mathbb{M}$, and σ_n denotes singular values that satisfy

$$\sigma_1>0\quad\text{and}\quad\sigma_n\approx0\quad\text{for}\quad n\geq2.$$

Then, $\{\mathbf{E}_1\}$ and $\{\mathbf{E}_2,\mathbf{E}_3,\cdots,\mathbf{E}_N\}$ are the (orthonormal) basis of the signal and null (or noise) space of $\mathbb{M}$, respectively. Therefore, one can define the projection operator onto the noise subspace. This projection is given explicitly by

$$\mathbb{P}_{\mathrm{noise}}=\mathbb{I}_N-\mathbf{E}_1\mathbf{E}_1^*,$$

where $\mathbb{I}_N$ denotes the $N\times N$ identity matrix. By regarding the structure of $\mathbb{E}(\mathbf{z})$ of (3.3), we introduce the following unit test vector $\mathbf{f}_\varepsilon(\mathbf{x},N)$: for $\mathbf{x}\in\Omega\subset\mathbb{R}^2$,

$$\mathbf{f}_\varepsilon(\mathbf{x},N)=\frac{1}{\sqrt{N}}\left[e^{ik_{\mathrm{b}}\boldsymbol{\theta}_1\cdot\mathbf{x}},e^{ik_{\mathrm{b}}\boldsymbol{\theta}_2\cdot\mathbf{x}},\ldots,e^{ik_{\mathrm{b}}\boldsymbol{\theta}_N\cdot\mathbf{x}}\right]^T, \tag{3.4}$$

where Ω denotes the region of interests (ROI). Then, there exists $N_0\in\mathbb{N}$ such that for any $N\geq N_0$, the following statement holds:

$$\mathbf{f}_\varepsilon(\mathbf{x},N)\in\text{Range}(\mathbb{M})\quad\text{if and only if}\quad\mathbf{x}=\mathbf{z}\in D.$$

This signifies that $\mathbb{P}_{\text{noise}}(\mathbf{f}_\varepsilon(\mathbf{x},N))=0$ when $\mathbf{z}\in D$. Thus, we can design a MUSIC-type imaging function such that

$$\mathfrak{F}_{\text{TM}}(\mathbf{x},N)=\frac{1}{|\mathbb{P}_{\text{noise}}(\mathbf{f}_\varepsilon(\mathbf{x},N))|}.$$

Then, the map of $\mathfrak{F}_{\text{TM}}(\mathbf{x},N)$ will have peaks of large ($+\infty$ in theory) and small amplitude at $\mathbf{x}\in D$ and $\mathbf{x}\in\Omega\backslash\overline{D}$, respectively.

Next, we assume that $\varepsilon(\mathbf{x})=\varepsilon_{\text{b}}$ and $\mu(\mathbf{x})\neq\mu_{\text{b}}$. Based on (2.1), since $u_\infty(\boldsymbol{\vartheta}_m,\boldsymbol{\theta}_n)$ can be approximated as

$$\begin{aligned}u_\infty(\boldsymbol{\vartheta}_m,\boldsymbol{\theta}_n)&\approx-\alpha^2\pi\frac{k_{\text{b}}^2(1+i)}{4\sqrt{k_{\text{b}}\pi}}\frac{2\mu_{\text{b}}}{\mu_{\text{a}}+\mu_{\text{b}}}(\boldsymbol{\vartheta}\cdot\boldsymbol{\theta})e^{-ik_{\text{b}}(\boldsymbol{\vartheta}-\boldsymbol{\theta})\cdot\mathbf{z}}\\&=-\alpha^2\pi\frac{k_{\text{b}}^2(1+i)}{4\sqrt{k_{\text{b}}\pi}}\frac{2\mu_{\text{b}}}{\mu_{\text{a}}+\mu_{\text{b}}}\left(\sum_{s=1}^{2}(\boldsymbol{\vartheta}\cdot\mathbf{e}_s)(\boldsymbol{\theta}\cdot\mathbf{e}_s)\right)e^{-ik_{\text{b}}(\boldsymbol{\vartheta}-\boldsymbol{\theta})\cdot\mathbf{z}},\end{aligned}$$

MSR matrix $\mathbb{M}$ can be written as

$$\mathbb{M}\approx\alpha^2\pi\frac{k_{\text{b}}^2(1+i)}{4\sqrt{k_{\text{b}}\pi}}\frac{2\mu_{\text{b}}}{\mu_{\text{a}}+\mu_{\text{b}}}\sum_{s=1}^{2}\mathbb{F}_s(\mathbf{z})^T\mathbb{F}_s(\mathbf{z}),\tag{3.5}$$

where

$$\begin{aligned}\mathbb{F}_s(\mathbf{z})&=\left[(-\boldsymbol{\vartheta}_1\cdot\mathbf{e}_s)e^{-ik_{\text{b}}\boldsymbol{\vartheta}_1\cdot\mathbf{z}},(-\boldsymbol{\vartheta}_2\cdot\mathbf{e}_s)e^{-ik_{\text{b}}\boldsymbol{\vartheta}_2\cdot\mathbf{z}},\ldots,(-\boldsymbol{\vartheta}_N\cdot\mathbf{e}_s)e^{-ik_{\text{b}}\boldsymbol{\vartheta}_N\cdot\mathbf{z}}\right]\Big|_{\boldsymbol{\vartheta}_m=-\boldsymbol{\theta}_m}\\&=\left[(\boldsymbol{\theta}_1\cdot\mathbf{e}_s)e^{ik_{\text{b}}\boldsymbol{\theta}_1\cdot\mathbf{z}},(\boldsymbol{\theta}_2\cdot\mathbf{e}_s)e^{ik_{\text{b}}\boldsymbol{\theta}_2\cdot\mathbf{z}},\ldots,(\boldsymbol{\theta}_N\cdot\mathbf{e}_s)e^{ik_{\text{b}}\boldsymbol{\theta}_N\cdot\mathbf{z}}\right].\end{aligned}\tag{3.6}$$

Based on the factorization of the MSR matrix, the range of $\mathbb{M}$ is determined by the span of $\{\mathbb{F}_1(\mathbf{z}),\mathbb{F}_2(\mathbf{z})\}$ corresponding to D. Thus, to introduce the imaging function of MUSIC, let us perform the singular value decomposition (SVD) of the MSR matrix $\mathbb{M}$:

$$\mathbb{M}=\sum_{n=1}^{N}\sigma_n\mathbf{E}_n\mathbf{F}_n^*\approx\sum_{n=1}^{2}\sigma_n\mathbf{E}_n\mathbf{F}_n^*.$$

Then, $\{\mathbf{E}_1,\mathbf{E}_2\}$ and $\{\mathbf{E}_3,\mathbf{E}_4,\cdots,\mathbf{E}_N\}$ are the (orthonormal) basis of the signal and null (or noise) space of $\mathbb{M}$, respectively. Therefore, one can define the projection operator onto the noise subspace. This projection is given explicitly by

$$\mathbb{P}_{\text{noise}}=\mathbb{I}_N-\sum_{n=1}^{2}\mathbf{E}_n\mathbf{E}_n^*.$$

By regarding the structure of $\mathbb{F}_s(\mathbf{z})$ of (3.6), we introduce the following unit test vector $\mathbf{f}_\mu(\mathbf{x},N)$: for $\mathbf{x}\in\Omega$ and $\boldsymbol{\xi}\in\mathbb{S}^1$,

$$\mathbf{f}_\mu(\mathbf{x},N)=\sqrt{\frac{2}{N}}\Big[(\boldsymbol{\theta}_1\cdot\boldsymbol{\xi})e^{ik_b\boldsymbol{\theta}_1\cdot\mathbf{x}},(\boldsymbol{\theta}_2\cdot\boldsymbol{\xi})e^{ik_b\boldsymbol{\theta}_2\cdot\mathbf{x}},\cdots,(\boldsymbol{\theta}_N\cdot\boldsymbol{\xi})e^{ik_b\boldsymbol{\theta}_N\cdot\mathbf{x}}\Big]^T, \tag{3.7}$$

where Ω denotes the region of interests (ROI). Then, there exists $N_0\in\mathbb{N}$ such that for any $N\geq N_0$, the following statement holds:

$$\mathbf{f}_\mu(\mathbf{x},N)\in\text{Range}(\mathbb{M})\quad\text{if and only if}\quad\mathbf{x}=\mathbf{z}\in D.$$

This signifies that $\mathbb{P}_{\text{noise}}(\mathbf{f}_\mu(\mathbf{x},N))=0$ when $\mathbf{z}\in D$. Thus, we can design a MUSIC-type imaging function such that

$$\mathfrak{F}_{\text{TE}}^{(\mu)}(\mathbf{x},N)=\frac{1}{|\mathbb{P}_{\text{noise}}(\mathbf{f}_\mu(\mathbf{x},N))|}.$$

Then, the map of $\mathfrak{F}_{\text{TE}}^{(\mu)}(\mathbf{x},N)$ will have peaks of large ($+\infty$ in theory) and small amplitude at $\mathbf{x}\in D$ and $\mathbf{x}\in\Omega\backslash\overline{D}$, respectively. A more detailed description is provided in [9].

Remark 3.1. Based on several studies [22,38,39,47], the selection of $\boldsymbol{\zeta}$ in (3.7) significantly depends on the shape of the unknown object. Unfortunately, since one has no *a priori* information about the shape of the object, a large number of directions $\boldsymbol{\zeta}_l$, $l=1,2,\cdots,L$, were applied at each search point and took the maximum value of $\mathfrak{F}_{\text{TE}}^{(\mu)}(\mathbf{x},N)$ among these directions. This process guarantees good imaging result but requires tremendous computational costs. Due to this reason, we set $\boldsymbol{\theta}_n\cdot\boldsymbol{\zeta}=1$ for all n, i.e., we apply the test vector $\mathbf{f}_\varepsilon(\mathbf{x},N)$ from (3.4) instead of (3.7) to introduce another imaging function for the MUSIC algorithm in the TE case such that

$$\mathfrak{F}_{\text{TE}}^{(\varepsilon)}(\mathbf{x},N)=\frac{1}{|\mathbb{P}_{\text{noise}}(\mathbf{f}_\varepsilon(\mathbf{x},N))|}.$$

4 MUSIC algorithm without diagonal elements of MSR matrix: Analysis and discussion

Hereinafter, we assume that we have no information of $u_\infty(\boldsymbol{\vartheta}_n,\boldsymbol{\theta}_n)$ for $n=1,2,\cdots,N$. That is, the obtained MSR matrix must be of the following form:

$$\mathbb{K}=\begin{bmatrix}\text{unknown} & u_\infty(\boldsymbol{\vartheta}_1,\boldsymbol{\theta}_2) & \cdots & u_\infty(\boldsymbol{\vartheta}_1,\boldsymbol{\theta}_{N-1}) & u_\infty(\boldsymbol{\vartheta}_1,\boldsymbol{\theta}_N)\\ u_\infty(\boldsymbol{\vartheta}_2,\boldsymbol{\theta}_1) & \text{unknown} & \cdots & u_\infty(\boldsymbol{\vartheta}_2,\boldsymbol{\theta}_{N-1}) & u_\infty(\boldsymbol{\vartheta}_2,\boldsymbol{\theta}_N)\\ \vdots & \vdots & \ddots & \vdots & \vdots\\ u_\infty(\boldsymbol{\vartheta}_N,\boldsymbol{\theta}_1) & u_\infty(\boldsymbol{\vartheta}_N,\boldsymbol{\theta}_2) & \cdots & u_\infty(\boldsymbol{\vartheta}_N,\boldsymbol{\theta}_{N-1}) & \text{unknown}\end{bmatrix}.$$

It should be noted that we have no any a priori information of the crack, and it is thus difficult to approximate the diagonal terms of the MSR matrix. Throughout this paper, we set the diagonal terms to be zero and consider the following MSR matrix:

$$\mathbb{K}=\begin{bmatrix} 0 & u_\infty(\boldsymbol{\vartheta}_1,\boldsymbol{\theta}_2) & \cdots & u_\infty(\boldsymbol{\vartheta}_1,\boldsymbol{\theta}_{N-1}) & u_\infty(\boldsymbol{\vartheta}_1,\boldsymbol{\theta}_N) \\ u_\infty(\boldsymbol{\vartheta}_2,\boldsymbol{\theta}_1) & 0 & \cdots & u_\infty(\boldsymbol{\vartheta}_2,\boldsymbol{\theta}_{N-1}) & u_\infty(\boldsymbol{\vartheta}_2,\boldsymbol{\theta}_N) \\ \vdots & \vdots & \ddots & \vdots & \vdots \\ u_\infty(\boldsymbol{\vartheta}_N,\boldsymbol{\theta}_1) & u_\infty(\boldsymbol{\vartheta}_N,\boldsymbol{\theta}_2) & \cdots & u_\infty(\boldsymbol{\vartheta}_N,\boldsymbol{\theta}_{N-1}) & 0 \end{bmatrix}. \tag{4.1}$$

The remaining part of the algorithm is identical to the traditional one. For TM case, since the SVD of $\mathbb{K}$ can be written as

$$\mathbb{K}=\sum_{n=1}^{N}\sigma_n\mathbf{U}_n\mathbf{V}_n^*\approx\sigma_1\mathbf{U}_1\mathbf{V}_1^*, \tag{4.2}$$

we can define the projection operator onto the noise subspace

$$\mathbb{P}_{\text{noise}}=\mathbb{I}_N-\mathbf{U}_1\mathbf{U}_1^*,$$

and introduce the MUSIC-type imaging function $\mathfrak{F}_{\text{DM}}$,

$$\mathfrak{F}_{\text{DM}}(\mathbf{x},N)=\frac{1}{|\mathbb{P}_{\text{noise}}(\mathbf{f}_\varepsilon(\mathbf{x},N))|}, \tag{4.3}$$

where $\mathbf{f}_\varepsilon(\mathbf{x},N)$ is defined in (3.4). Then surprisingly, the location of $\mathbf{z}\in D$ can be identified through the map of $\mathfrak{F}_{\text{DM}}(\mathbf{x},N)$ when the total number of incident/observation directions N is sufficiently large.

Remark 4.1. Although, the diagonal elements of the $\mathbb{K}$ are missing, total number of nonzero singular values is same as the total number of cracks but structure of singular values is quiet different from the ones of $\mathbb{M}$. This fact has been examined heuristically in [42].

For TE case, since the SVD of $\mathbb{K}$ can be written as

$$\mathbb{K}=\sum_{n=1}^{N}\sigma_n\mathbf{U}_n\mathbf{V}_n^*\approx\sum_{n=1}^{2}\sigma_n\mathbf{U}_n\mathbf{V}_n^*, \tag{4.4}$$

we can define the projection operator onto the noise subspace

$$\mathbb{P}_{\text{noise}}=\mathbb{I}_N-\sum_{n=1}^{2}\mathbf{U}_n\mathbf{U}_n^*.$$

With this and based on the Remark 3.1, corresponding imaging functions of the MUSIC can be introduced

$$\mathfrak{F}_{\text{DE}}^{(\varepsilon)}(\mathbf{x},N)=\frac{1}{|\mathbb{P}_{\text{noise}}(\mathbf{f}_\varepsilon(\mathbf{x}))|}\quad\text{and}\quad\mathfrak{F}_{\text{DE}}^{(\mu)}(\mathbf{x},N)=\frac{1}{|\mathbb{P}_{\text{noise}}(\mathbf{f}_\mu(\mathbf{x}))|}. \tag{4.5}$$

To confirm the applicability of MUSIC in both TM and TE cases, we establish mathematical structures of (4.3) and (4.5) by identifying a relationship with Bessel functions.

4.1 Structure of the imaging function: TM case

For proper analysis, we introduce a result derived in [39] that plays an important role in our analysis.

Lemma 4.1. *For sufficiently large N, $\boldsymbol{\theta}_n \in \mathbb{S}^1$ in* (3.1)*, and $\mathbf{x} \in \mathbb{R}^2$,*

$$\frac{1}{N}\sum_{n=1}^{N} e^{ik_{\mathrm{b}}\boldsymbol{\theta}_n\cdot\mathbf{x}} \approx J_0(k_{\mathrm{b}}|\mathbf{x}|), \tag{4.6}$$

where J_n denotes the Bessel function of order n of the first kind.

Now, we derive the following result about the structure of $\mathfrak{F}_{\mathrm{DM}}(\mathbf{x},N)$.

Theorem 4.1 (TM polarization case)**.** *For sufficiently large N and k_{b}, $\mathfrak{F}_{\mathrm{DM}}(\mathbf{x},N)$ can be represented as follows:*

$$\mathfrak{F}_{\mathrm{DM}}(\mathbf{x},N) \approx \left(\frac{N^2-2N+1}{N^2-2N}\right)\left(1-J_0(k_{\mathrm{b}}|\mathbf{x}-\mathbf{z}|)^2\right)^{-1/2}. \tag{4.7}$$

Proof. Based on (3.2), (4.1), and (4.2), $\mathbb{K}$ can be written

$$\mathbb{K} \approx \frac{\alpha^2 k_{\mathrm{b}}^2(1+i)(\varepsilon_{\mathrm{a}}-\varepsilon_{\mathrm{b}})\pi}{4\sqrt{k_{\mathrm{b}}\pi\varepsilon_{\mathrm{b}}\mu_{\mathrm{b}}}}\begin{bmatrix} 0 & e^{ik_{\mathrm{b}}(\boldsymbol{\theta}_1+\boldsymbol{\theta}_2)\cdot\mathbf{z}} & \cdots & e^{ik_{\mathrm{b}}(\boldsymbol{\theta}_1+\boldsymbol{\theta}_N)\cdot\mathbf{z}} \\ e^{ik_{\mathrm{b}}(\boldsymbol{\theta}_2+\boldsymbol{\theta}_1)\cdot\mathbf{z}} & 0 & \cdots & e^{ik_{\mathrm{b}}(\boldsymbol{\theta}_2+\boldsymbol{\theta}_N)\cdot\mathbf{z}} \\ \vdots & \vdots & \ddots & \vdots \\ e^{ik_{\mathrm{b}}(\boldsymbol{\theta}_N+\boldsymbol{\theta}_1)\cdot\mathbf{z}} & e^{ik_{\mathrm{b}}(\boldsymbol{\theta}_N+\boldsymbol{\theta}_2)\cdot\mathbf{z}} & \cdots & 0 \end{bmatrix}.$$

Then, performing an elementary calculus yields

$$\frac{1}{(\sigma_1)^2}\mathbb{K}\mathbb{K}^* \approx C_\varepsilon\begin{bmatrix} N-1 & (N-2)e^{ik_{\mathrm{b}}(\boldsymbol{\theta}_1-\boldsymbol{\theta}_2)\cdot\mathbf{z}} & \cdots & (N-2)e^{ik_{\mathrm{b}}(\boldsymbol{\theta}_1-\boldsymbol{\theta}_N)\cdot\mathbf{z}} \\ (N-2)e^{ik_{\mathrm{b}}(\boldsymbol{\theta}_2-\boldsymbol{\theta}_1)\cdot\mathbf{z}} & N-1 & \cdots & (N-2)e^{ik_{\mathrm{b}}(\boldsymbol{\theta}_2-\boldsymbol{\theta}_N)\cdot\mathbf{z}} \\ \vdots & \vdots & \ddots & \vdots \\ (N-2)e^{ik_{\mathrm{b}}(\boldsymbol{\theta}_N-\boldsymbol{\theta}_1)\cdot\mathbf{z}} & (N-2)e^{ik_{\mathrm{b}}(\boldsymbol{\theta}_N-\boldsymbol{\theta}_2)\cdot\mathbf{z}} & \cdots & N-1 \end{bmatrix},$$

where

$$C_\varepsilon = \left(\frac{\alpha^2 k_{\mathrm{b}}^2(\varepsilon_{\mathrm{a}}-\varepsilon_{\mathrm{b}})\pi}{2\sigma_1\sqrt{k_{\mathrm{b}}\pi\varepsilon_{\mathrm{b}}\mu_{\mathrm{b}}}}\right)^2.$$

Then, we have

$$\begin{aligned}\mathbb{I}-\mathbf{U}_1\mathbf{U}_1^* &= \mathbb{I}-\frac{1}{(\sigma_1)^2}\mathbb{K}\mathbb{K}^* \\ &\approx (1-C_\varepsilon)\mathbb{I}-C_\varepsilon(N-2)\begin{bmatrix} e^{ik_{\mathrm{b}}(\boldsymbol{\theta}_1-\boldsymbol{\theta}_1)\cdot\mathbf{z}} & e^{ik_{\mathrm{b}}(\boldsymbol{\theta}_1-\boldsymbol{\theta}_2)\cdot\mathbf{z}} & \cdots & e^{ik_{\mathrm{b}}(\boldsymbol{\theta}_1-\boldsymbol{\theta}_N)\cdot\mathbf{z}} \\ e^{ik_{\mathrm{b}}(\boldsymbol{\theta}_2-\boldsymbol{\theta}_1)\cdot\mathbf{z}} & e^{ik_{\mathrm{b}}(\boldsymbol{\theta}_2-\boldsymbol{\theta}_2)\cdot\mathbf{z}} & \cdots & e^{ik_{\mathrm{b}}(\boldsymbol{\theta}_2-\boldsymbol{\theta}_N)\cdot\mathbf{z}} \\ \vdots & \vdots & \ddots & \vdots \\ e^{ik_{\mathrm{b}}(\boldsymbol{\theta}_N-\boldsymbol{\theta}_1)\cdot\mathbf{z}} & e^{ik_{\mathrm{b}}(\boldsymbol{\theta}_N-\boldsymbol{\theta}_2)\cdot\mathbf{z}} & \cdots & e^{ik_{\mathrm{b}}(\boldsymbol{\theta}_N-\boldsymbol{\theta}_N)\cdot\mathbf{z}} \end{bmatrix}.\end{aligned}$$

Based on (4.6), since

$$e^{ik_b\boldsymbol{\theta}_p\cdot\mathbf{z}}\sum_{n=1}^{N}e^{ik_b\boldsymbol{\theta}_n\cdot(\mathbf{x}-\mathbf{z})}\approx Ne^{ik_b\boldsymbol{\theta}_p\cdot\mathbf{z}}J_0(k_b|\mathbf{x}-\mathbf{z}|) \tag{4.8}$$

for $p=1,2,\cdots,N$, we have

$$\begin{bmatrix} e^{ik_b(\boldsymbol{\theta}_1-\boldsymbol{\theta}_1)\cdot\mathbf{z}} & e^{ik_b(\boldsymbol{\theta}_1-\boldsymbol{\theta}_2)\cdot\mathbf{z}} & \cdots & e^{ik_b(\boldsymbol{\theta}_1-\boldsymbol{\theta}_N)\cdot\mathbf{z}} \\ e^{ik_b(\boldsymbol{\theta}_2-\boldsymbol{\theta}_1)\cdot\mathbf{z}} & e^{ik_b(\boldsymbol{\theta}_2-\boldsymbol{\theta}_2)\cdot\mathbf{z}} & \cdots & e^{ik_b(\boldsymbol{\theta}_2-\boldsymbol{\theta}_N)\cdot\mathbf{z}} \\ \vdots & \vdots & \ddots & \vdots \\ e^{ik_b(\boldsymbol{\theta}_N-\boldsymbol{\theta}_1)\cdot\mathbf{z}} & e^{ik_b(\boldsymbol{\theta}_N-\boldsymbol{\theta}_2)\cdot\mathbf{z}} & \cdots & e^{ik_b(\boldsymbol{\theta}_N-\boldsymbol{\theta}_N)\cdot\mathbf{z}} \end{bmatrix}\begin{bmatrix} e^{ik_b\boldsymbol{\theta}_1\cdot\mathbf{x}} \\ e^{ik_b\boldsymbol{\theta}_2\cdot\mathbf{x}} \\ \vdots \\ e^{ik_b\boldsymbol{\theta}_N\cdot\mathbf{x}} \end{bmatrix}\approx\begin{bmatrix} Ne^{ik_b\boldsymbol{\theta}_1\cdot\mathbf{z}}J_0(k_b|\mathbf{x}-\mathbf{z}|) \\ Ne^{ik_b\boldsymbol{\theta}_2\cdot\mathbf{z}}J_0(k_b|\mathbf{x}-\mathbf{z}|) \\ \vdots \\ Ne^{ik_b\boldsymbol{\theta}_N\cdot\mathbf{z}}J_0(k_b|\mathbf{x}-\mathbf{z}|) \end{bmatrix}$$

and correspondingly,

$$\begin{aligned}\mathbb{P}_{\text{noise}}(\mathbf{f}_\varepsilon(\mathbf{x},N)) &= (\mathbb{I}-\mathbf{U}_1\mathbf{U}_1^*)\mathbf{f}_\varepsilon(\mathbf{x},N)\\ &\approx\frac{1-C_\varepsilon}{\sqrt{N}}\begin{bmatrix} e^{ik_b\boldsymbol{\theta}_1\cdot\mathbf{x}} \\ e^{ik_b\boldsymbol{\theta}_2\cdot\mathbf{x}} \\ \vdots \\ e^{ik_b\boldsymbol{\theta}_N\cdot\mathbf{x}} \end{bmatrix}-C_\varepsilon(N-2)\sqrt{N}\begin{bmatrix} e^{ik_b\boldsymbol{\theta}_1\cdot\mathbf{z}}J_0(k_b|\mathbf{x}-\mathbf{z}|) \\ e^{ik_b\boldsymbol{\theta}_2\cdot\mathbf{z}}J_0(k_b|\mathbf{x}-\mathbf{z}|) \\ \vdots \\ e^{ik_b\boldsymbol{\theta}_N\cdot\mathbf{z}}J_0(k_b|\mathbf{x}-\mathbf{z}|) \end{bmatrix}.\end{aligned}$$

Now, let us write

$$\begin{aligned}|\mathbb{P}_{\text{noise}}(\mathbf{f}_\varepsilon(\mathbf{x},N))| &= \left(\mathbb{P}_{\text{noise}}(\mathbf{f}_\varepsilon(\mathbf{x},N))\cdot\overline{\mathbb{P}_{\text{noise}}(\mathbf{f}_\varepsilon(\mathbf{x},N))}\right)^{1/2}\\ &= \left(\sum_{n=1}^{N}\left(\frac{(1-C_\varepsilon)^2}{N}-\left(\Psi_1(\mathbf{x},n)+\overline{\Psi_1(\mathbf{x},n)}\right)+\Psi_2(\mathbf{x},n)\overline{\Psi_2(\mathbf{x},n)}\right)\right)^{1/2},\end{aligned}$$

where

$$\begin{aligned}\Psi_1(\mathbf{x},n) &= (1-C_\varepsilon)C_\varepsilon(N-2)e^{ik_b\boldsymbol{\theta}_n\cdot(\mathbf{x}-\mathbf{z})}J_0(k_b|\mathbf{x}-\mathbf{z}|),\\ \Psi_2(\mathbf{x},n) &= C_\varepsilon(N-2)\sqrt{N}e^{ik_b\boldsymbol{\theta}_n\cdot\mathbf{z}}J_0(k_b|\mathbf{x}-\mathbf{z}|).\end{aligned}$$

Applying (4.8) again, we can obtain

$$\sum_{n=1}^{N}\left(\Psi_1(\mathbf{x},n)+\overline{\Psi_1(\mathbf{x},n)}\right)=2C_\varepsilon(1-C_\varepsilon)(N-2)NJ_0(k_b|\mathbf{x}-\mathbf{z}|)^2$$

and

$$\sum_{n=1}^{N}\Psi_2(\mathbf{x},n)\overline{\Psi_2(\mathbf{x},n)}=C_\varepsilon^2(N-2)^2N^2J_0(k_b|\mathbf{x}-\mathbf{z}|)^2.$$

Hence, $|\mathbb{P}_{\text{noise}}(\mathbf{f}_\varepsilon(\mathbf{x},N))|$ becomes

$$\begin{aligned}&|\mathbb{P}_{\text{noise}}(\mathbf{f}_\varepsilon(\mathbf{x},N))|\\ =&\Big((1-C_\varepsilon)^2-2(1-C_\varepsilon)C_\varepsilon(N-2)NJ_0(k_\text{b}|\mathbf{x}-\mathbf{z}|)^2+C_\varepsilon^2(N-2)^2N^2J_0(k_\text{b}|\mathbf{x}-\mathbf{z}|)^2\Big)^{1/2}.\end{aligned}$$

Since $|\mathbb{P}_{\text{noise}}(\mathbf{f}_\varepsilon(\mathbf{z}))|=0$ and $J_0(0)=1$,

$$(1-C_\varepsilon)^2-2(1-C_\varepsilon)C_\varepsilon(N-2)N+C_\varepsilon^2(N-2)^2N^2=\Big((1-C_\varepsilon)-C_\varepsilon N(N-2)\Big)^2=0.$$

This implies that $C_\varepsilon=(N-1)^{-2}$ and correspondingly,

$$\begin{aligned}|\mathbb{P}_{\text{noise}}(\mathbf{f}_\varepsilon(\mathbf{x},N))|&\approx(1-C_\varepsilon)\Big(1-J_0(k_\text{b}|\mathbf{x}-\mathbf{z}|)^2\Big)^{1/2}\\ &=\left(\frac{N^2-2N}{N^2-2N+1}\right)\Big(1-J_0(k_\text{b}|\mathbf{x}-\mathbf{z}|)^2\Big)^{1/2}.\end{aligned}$$

Hence, we can derive the (4.7). □

Based on the identified structure (4.7), we can observe several properties of MUSIC.

Remark 4.2 (Applicability of MUSIC)**.** Since $J_0(0)=1$, the map of $\mathfrak{F}_{\text{DM}}(\mathbf{x},N)$ will contain peak of large magnitude (theoretically $+\infty$) at $\mathbf{x}=\mathbf{z}\in D$. This explains why MUSIC is applicable for imaging or identifying cracks without diagonal elements of an MSR matrix.

Remark 4.3 (Resolution of imaging results)**.** As in traditional MUSIC-type imaging, the resolution of the imaging result is highly dependent on the values of k_b and N. This signifies that because $\mathfrak{F}_{\text{DM}}(\mathbf{x},N)$ is related to J_0, a result of poor resolution will obtained if k_b is small. In contrast, if k_b is sufficiently large (as we assume in Theorem 4.1), a result of high resolution can be obtained even in the presence of various artifacts.

Remark 4.4 (Influence of total number of incident/observation directions)**.** Based on recent work [38, Section 3.5], $\mathfrak{F}_{\text{TM}}(\mathbf{x},N)$ satisfies

$$\lim_{N\to\infty}\mathfrak{F}_{\text{TM}}(\mathbf{x},N)=\Big(1-J_0(k_\text{b}|\mathbf{x}-\mathbf{z}|)^2\Big)^{-1/2}.$$

Since

$$\begin{aligned}\lim_{N\to\infty}\mathfrak{F}_{\text{DM}}(\mathbf{x},N)&=\lim_{N\to\infty}\left(\frac{N^2-2N+1}{N^2-2N}\right)\Big(1-J_0(k_\text{b}|\mathbf{x}-\mathbf{z}|)^2\Big)^{-1/2}\\ &=\Big(1-J_0(k_\text{b}|\mathbf{x}-\mathbf{z}|)^2\Big)^{-1/2}=\lim_{N\to\infty}\mathfrak{F}_{\text{TM}}(\mathbf{x},N),\end{aligned}$$

we can examine that sufficiently large number of incident/observation directions should be applied to increase the resolution of the imaging results, i.e, a result of poor resolution will appear if N is small.

Based on the Remark 4.2, we can also examine the unique determination.

Corollary 4.1 (Unique determination of object)**.** *For sufficiently large N and k_b, the location of small object can be identified uniquely via the map of $\mathfrak{F}_{\text{DM}}(\mathbf{x},N)$.*

4.2 Structure of the imaging function: TE case

Now, we analyze the imaging function in TE polarization. We first recall a useful result derived in [39,40].

Lemma 4.2. *For sufficiently large N, $\boldsymbol{\theta}_n \in \mathbb{S}^1$ in* (3.1), *$\boldsymbol{\xi} \in \mathbb{S}^1$, and $\mathbf{x} \in \mathbb{R}^2 \setminus \{\mathbf{0}\}$,*

$$\begin{aligned}
\frac{1}{N}\sum_{n=1}^{N}(\boldsymbol{\xi}\cdot\boldsymbol{\theta}_n)e^{ik_{\mathrm{b}}\boldsymbol{\theta}_n\cdot\mathbf{x}} &\approx i\left(\frac{\mathbf{x}}{|\mathbf{x}|}\cdot\boldsymbol{\xi}\right)J_1(k_{\mathrm{b}}|\mathbf{x}|),\\
\frac{1}{N}\sum_{n=1}^{N}(\boldsymbol{\xi}\cdot\boldsymbol{\theta}_n)^2e^{ik_{\mathrm{b}}\boldsymbol{\theta}_n\cdot\mathbf{x}} &\approx \frac{1}{2}\Big(J_0(k_{\mathrm{b}}|\mathbf{x}|)+J_2(k_{\mathrm{b}}|\mathbf{x}|)\Big)-\left(\frac{\mathbf{x}}{|\mathbf{x}|}\cdot\boldsymbol{\xi}\right)^2 J_2(k_{\mathrm{b}}|\mathbf{x}|),\\
\frac{1}{N}\sum_{n=1}^{N}(\boldsymbol{\theta}_m\cdot\boldsymbol{\theta}_n)(\boldsymbol{\xi}\cdot\boldsymbol{\theta}_n)e^{ik_{\mathrm{b}}\boldsymbol{\theta}_n\cdot\mathbf{x}} &\approx \frac{1}{2}(\boldsymbol{\theta}_m\cdot\boldsymbol{\xi})\Big(J_0(k_{\mathrm{b}}|\mathbf{x}|)+J_2(k_{\mathrm{b}}|\mathbf{x}|)\Big)\\
&\quad-\left(\frac{\mathbf{x}}{|\mathbf{x}|}\cdot\boldsymbol{\theta}_m\right)\left(\frac{\mathbf{x}}{|\mathbf{x}|}\cdot\boldsymbol{\xi}\right)J_2(k_{\mathrm{b}}|\mathbf{x}|).
\end{aligned} \tag{4.9}$$

If $\mathbf{x}=\mathbf{0}$ then

$$\frac{1}{N}\sum_{n=1}^{N}(\boldsymbol{\xi}\cdot\boldsymbol{\theta}_n)\approx 0,\quad \frac{1}{N}\sum_{n=1}^{N}(\boldsymbol{\xi}\cdot\boldsymbol{\theta}_n)^2\approx\frac{1}{2},\quad \text{and}\quad \frac{1}{N}\sum_{n=1}^{N}(\boldsymbol{\theta}_m\cdot\boldsymbol{\theta}_n)(\boldsymbol{\xi}\cdot\boldsymbol{\theta}_n)\approx\frac{1}{2}(\boldsymbol{\theta}_m\cdot\boldsymbol{\xi}).$$

Now, we derive the following result about the structures of $\mathfrak{F}_{\mathrm{DE}}^{(\varepsilon)}(\mathbf{x},N)$ and $\mathfrak{F}_{\mathrm{DE}}^{(\varepsilon)}(\mathbf{x},N)$.

Theorem 4.2 (TE polarization case)**.** *Let $\boldsymbol{\xi}=(\cos\xi,\sin\xi)$. Then, for sufficiently large N and k_{b}, $\mathfrak{F}_{\mathrm{DE}}^{(\varepsilon)}(\mathbf{x},N)$ and $\mathfrak{F}_{\mathrm{DE}}^{(\mu)}(\mathbf{x},N)$ can be represented as follows:*

$$\begin{aligned}
\mathfrak{F}_{\mathrm{DE}}^{(\varepsilon)}(\mathbf{x},N)\approx\Bigg((1-C_\mu)^2-2C_\mu(1-C_\mu)N\left(\frac{N}{2}-2\right)J_1(k_{\mathrm{b}}|\mathbf{x}-\mathbf{z}|)^2\\
+C_\mu^2\frac{N^2}{2}\left(\frac{N}{2}-2\right)^2 J_1(k_{\mathrm{b}}|\mathbf{x}-\mathbf{z}|)^2\Bigg)^{-1/2}
\end{aligned} \tag{4.10}$$

and

$$\begin{aligned}
\mathfrak{F}_{\mathrm{DE}}^{(\mu)}(\mathbf{x},N)\approx\Bigg((1-C_\mu)^2-2(1-C_\mu)C_\mu N\left(\frac{N}{2}-2\right)\Psi(\mathbf{x},\mathbf{z})\\
+C_\mu^2N^2\left(\frac{N}{2}-2\right)^2\Psi(\mathbf{x},\mathbf{z})\Bigg)^{-1/2},
\end{aligned} \tag{4.11}$$

where $\sigma_1\approx\sigma_2=\sigma$,

$$C_\mu=\left(\frac{\alpha^2k_{\mathrm{b}}^2\mu_{\mathrm{b}}\pi}{\sigma(\mu_{\mathrm{a}}+\mu_{\mathrm{b}})\sqrt{k_{\mathrm{b}}\pi}}\right)^2,$$

and

$$\begin{aligned}\Psi(\mathbf{x},\mathbf{z}) = &\frac{1}{4}\Big(J_0(k_\mathrm{b}|\mathbf{x}-\mathbf{z}|)+J_2(k_\mathrm{b}|\mathbf{x}-\mathbf{z}|)\Big)^2\\ &-\left(\frac{\mathbf{x}-\mathbf{z}}{|\mathbf{x}-\mathbf{z}|}\cdot\boldsymbol{\xi}\right)^2\Big(J_0(k_\mathrm{b}|\mathbf{x}-\mathbf{z}|)+J_2(k_\mathrm{b}|\mathbf{x}-\mathbf{z}|)\Big)J_2(k_\mathrm{b}|\mathbf{x}-\mathbf{z}|)\\ &+\left(\frac{\mathbf{x}-\mathbf{z}}{|\mathbf{x}-\mathbf{z}|}\cdot\boldsymbol{\xi}\right)^2 J_2(k_\mathrm{b}|\mathbf{x}-\mathbf{z}|)^2.\end{aligned}$$

Proof. Based on (3.5), (4.1), and (4.4), $\mathbb{K}$ can be written

$$\mathbb{K}\approx\frac{\alpha^2k_\mathrm{b}^2(1+i)\mu_\mathrm{b}\pi}{2(\mu_\mathrm{a}+\mu_\mathrm{b})\sqrt{k_\mathrm{b}\pi}}\begin{bmatrix}0 & (\boldsymbol{\theta}_1\cdot\boldsymbol{\theta}_2)e^{ik_\mathrm{b}(\boldsymbol{\theta}_1+\boldsymbol{\theta}_2)\cdot\mathbf{z}} & \cdots & (\boldsymbol{\theta}_1\cdot\boldsymbol{\theta}_N)e^{ik_\mathrm{b}(\boldsymbol{\theta}_1+\boldsymbol{\theta}_N)\cdot\mathbf{z}}\\ (\boldsymbol{\theta}_2\cdot\boldsymbol{\theta}_1)e^{ik_\mathrm{b}(\boldsymbol{\theta}_2+\boldsymbol{\theta}_1)\cdot\mathbf{z}} & 0 & \cdots & (\boldsymbol{\theta}_2\cdot\boldsymbol{\theta}_N)e^{ik_\mathrm{b}(\boldsymbol{\theta}_2+\boldsymbol{\theta}_N)\cdot\mathbf{z}}\\ \vdots & \vdots & \ddots & \vdots\\ (\boldsymbol{\theta}_N\cdot\boldsymbol{\theta}_1)e^{ik_\mathrm{b}(\boldsymbol{\theta}_N+\boldsymbol{\theta}_1)\cdot\mathbf{z}} & (\boldsymbol{\theta}_N\cdot\boldsymbol{\theta}_2)e^{ik_\mathrm{b}(\boldsymbol{\theta}_N+\boldsymbol{\theta}_2)\cdot\mathbf{z}} & \cdots & 0\end{bmatrix}.$$

Since $\sigma_1\approx\sigma_2=\sigma$, by letting $\mathcal{N}(n,m)=(N/2-2)(\boldsymbol{\theta}_n\cdot\boldsymbol{\theta}_m)$, we have

$$\frac{1}{\sigma^2}\mathbb{K}\mathbb{K}^*\approx C_\mu\begin{bmatrix}N/2-1 & \mathcal{N}(1,2)e^{ik_\mathrm{b}(\boldsymbol{\theta}_1-\boldsymbol{\theta}_2)\cdot\mathbf{z}} & \cdots & \mathcal{N}(1,N)e^{ik_\mathrm{b}(\boldsymbol{\theta}_1-\boldsymbol{\theta}_N)\cdot\mathbf{z}}\\ \mathcal{N}(2,1)e^{ik_\mathrm{b}(\boldsymbol{\theta}_2-\boldsymbol{\theta}_1)\cdot\mathbf{z}} & N/2-1 & \cdots & \mathcal{N}(2,N)e^{ik_\mathrm{b}(\boldsymbol{\theta}_2-\boldsymbol{\theta}_N)\cdot\mathbf{z}}\\ \vdots & \vdots & \ddots & \vdots\\ \mathcal{N}(N,1)e^{ik_\mathrm{b}(\boldsymbol{\theta}_N-\boldsymbol{\theta}_1)\cdot\mathbf{z}} & \mathcal{N}(N,2)e^{ik_\mathrm{b}(\boldsymbol{\theta}_N-\boldsymbol{\theta}_2)\cdot\mathbf{z}} & \cdots & N/2-1\end{bmatrix}$$

and correspondingly,

$$\begin{aligned}\mathbb{I}-\sum_{m=1}^{2}\mathbf{U}_m\mathbf{U}_m^* &= \mathbb{I}-\frac{1}{\sigma^2}\mathbb{K}\mathbb{K}^*\approx(1-C_\mu)\mathbb{I}\\ &-C_\mu\left(\frac{N}{2}-2\right)\begin{bmatrix}(\boldsymbol{\theta}_1\cdot\boldsymbol{\theta}_1)e^{ik_\mathrm{b}(\boldsymbol{\theta}_1-\boldsymbol{\theta}_1)\cdot\mathbf{z}} & (\boldsymbol{\theta}_1\cdot\boldsymbol{\theta}_2)e^{ik_\mathrm{b}(\boldsymbol{\theta}_1-\boldsymbol{\theta}_2)\cdot\mathbf{z}} & \cdots & (\boldsymbol{\theta}_1\cdot\boldsymbol{\theta}_N)e^{ik_\mathrm{b}(\boldsymbol{\theta}_1-\boldsymbol{\theta}_N)\cdot\mathbf{z}}\\ (\boldsymbol{\theta}_2\cdot\boldsymbol{\theta}_1)e^{ik_\mathrm{b}(\boldsymbol{\theta}_2-\boldsymbol{\theta}_1)\cdot\mathbf{z}} & (\boldsymbol{\theta}_2\cdot\boldsymbol{\theta}_2)e^{ik_\mathrm{b}(\boldsymbol{\theta}_2-\boldsymbol{\theta}_2)\cdot\mathbf{z}} & \cdots & (\boldsymbol{\theta}_2\cdot\boldsymbol{\theta}_N)e^{ik_\mathrm{b}(\boldsymbol{\theta}_2-\boldsymbol{\theta}_N)\cdot\mathbf{z}}\\ \vdots & \vdots & \ddots & \vdots\\ (\boldsymbol{\theta}_N\cdot\boldsymbol{\theta}_1)e^{ik_\mathrm{b}(\boldsymbol{\theta}_N-\boldsymbol{\theta}_1)\cdot\mathbf{z}} & (\boldsymbol{\theta}_N\cdot\boldsymbol{\theta}_2)e^{ik_\mathrm{b}(\boldsymbol{\theta}_N-\boldsymbol{\theta}_2)\cdot\mathbf{z}} & \cdots & (\boldsymbol{\theta}_N\cdot\boldsymbol{\theta}_N)e^{ik_\mathrm{b}(\boldsymbol{\theta}_N-\boldsymbol{\theta}_N)\cdot\mathbf{z}}\end{bmatrix}.\end{aligned}$$

First, we consider the structure of $\mathbb{P}_{\text{noise}}(\mathbf{f}_\varepsilon(\mathbf{x},N))$. Based on (4.9), since

$$\begin{bmatrix} (\boldsymbol{\theta}_1\cdot\boldsymbol{\theta}_1)e^{ik_b(\boldsymbol{\theta}_1-\boldsymbol{\theta}_1)\cdot\mathbf{z}} & (\boldsymbol{\theta}_1\cdot\boldsymbol{\theta}_2)e^{ik_b(\boldsymbol{\theta}_1-\boldsymbol{\theta}_2)\cdot\mathbf{z}} & \cdots & (\boldsymbol{\theta}_1\cdot\boldsymbol{\theta}_N)e^{ik_b(\boldsymbol{\theta}_1-\boldsymbol{\theta}_N)\cdot\mathbf{z}} \\ (\boldsymbol{\theta}_2\cdot\boldsymbol{\theta}_1)e^{ik_b(\boldsymbol{\theta}_2-\boldsymbol{\theta}_1)\cdot\mathbf{z}} & (\boldsymbol{\theta}_2\cdot\boldsymbol{\theta}_2)e^{ik_b(\boldsymbol{\theta}_2-\boldsymbol{\theta}_2)\cdot\mathbf{z}} & \cdots & (\boldsymbol{\theta}_2\cdot\boldsymbol{\theta}_N)e^{ik_b(\boldsymbol{\theta}_2-\boldsymbol{\theta}_N)\cdot\mathbf{z}} \\ \vdots & \vdots & \ddots & \vdots \\ (\boldsymbol{\theta}_N\cdot\boldsymbol{\theta}_1)e^{ik_b(\boldsymbol{\theta}_N-\boldsymbol{\theta}_1)\cdot\mathbf{z}} & (\boldsymbol{\theta}_N\cdot\boldsymbol{\theta}_2)e^{ik_b(\boldsymbol{\theta}_N-\boldsymbol{\theta}_2)\cdot\mathbf{z}} & \cdots & (\boldsymbol{\theta}_N\cdot\boldsymbol{\theta}_N)e^{ik_b(\boldsymbol{\theta}_N-\boldsymbol{\theta}_N)\cdot\mathbf{z}} \end{bmatrix} \begin{bmatrix} e^{ik_b\boldsymbol{\theta}_1\cdot\mathbf{x}} \\ e^{ik_b\boldsymbol{\theta}_2\cdot\mathbf{x}} \\ \vdots \\ e^{ik_b\boldsymbol{\theta}_N\cdot\mathbf{x}} \end{bmatrix}$$

$$= \begin{bmatrix} e^{ik_b\boldsymbol{\theta}_1\cdot\mathbf{z}}\sum_{n=1}^{N}(\boldsymbol{\theta}_1\cdot\boldsymbol{\theta}_n)e^{ik_b\boldsymbol{\theta}_n\cdot(\mathbf{x}-\mathbf{z})} \\ e^{ik_b\boldsymbol{\theta}_2\cdot\mathbf{z}}\sum_{n=1}^{N}(\boldsymbol{\theta}_2\cdot\boldsymbol{\theta}_n)e^{ik_b\boldsymbol{\theta}_n\cdot(\mathbf{x}-\mathbf{z})} \\ \vdots \\ e^{ik_b\boldsymbol{\theta}_N\cdot\mathbf{z}}\sum_{n=1}^{N}(\boldsymbol{\theta}_N\cdot\boldsymbol{\theta}_n)e^{ik_b\boldsymbol{\theta}_n\cdot(\mathbf{x}-\mathbf{z})} \end{bmatrix} \approx \begin{bmatrix} iNe^{ik_b\boldsymbol{\theta}_1\cdot\mathbf{z}}\left(\frac{\mathbf{x}-\mathbf{z}}{|\mathbf{x}-\mathbf{z}|}\cdot\boldsymbol{\theta}_1\right)J_1(k_b|\mathbf{x}-\mathbf{z}|) \\ iNe^{ik_b\boldsymbol{\theta}_2\cdot\mathbf{z}}\left(\frac{\mathbf{x}-\mathbf{z}}{|\mathbf{x}-\mathbf{z}|}\cdot\boldsymbol{\theta}_2\right)J_1(k_b|\mathbf{x}-\mathbf{z}|) \\ \vdots \\ iNe^{ik_b\boldsymbol{\theta}_N\cdot\mathbf{z}}\left(\frac{\mathbf{x}-\mathbf{z}}{|\mathbf{x}-\mathbf{z}|}\cdot\boldsymbol{\theta}_N\right)J_1(k_b|\mathbf{x}-\mathbf{z}|) \end{bmatrix},$$

we can examine that

$$\mathbb{P}_{\text{noise}}(\mathbf{f}_\varepsilon(\mathbf{x},N)) = \left(\mathbb{I}-\sum_{m=1}^{2}\mathbf{U}_m\mathbf{U}_m^*\right)\mathbf{f}_\varepsilon(\mathbf{x})$$

$$\approx \frac{1-C_\mu}{\sqrt{N}}\begin{bmatrix} e^{ik_b\boldsymbol{\theta}_1\cdot\mathbf{x}} \\ e^{ik_b\boldsymbol{\theta}_2\cdot\mathbf{x}} \\ \vdots \\ e^{ik_b\boldsymbol{\theta}_N\cdot\mathbf{x}} \end{bmatrix} - iC_\mu\left(\frac{N}{2}-2\right)\sqrt{N}\begin{bmatrix} e^{ik_b\boldsymbol{\theta}_1\cdot\mathbf{z}}\left(\frac{\mathbf{x}-\mathbf{z}}{|\mathbf{x}-\mathbf{z}|}\cdot\boldsymbol{\theta}_1\right)J_1(k_b|\mathbf{x}-\mathbf{z}|) \\ e^{ik_b\boldsymbol{\theta}_2\cdot\mathbf{z}}\left(\frac{\mathbf{x}-\mathbf{z}}{|\mathbf{x}-\mathbf{z}|}\cdot\boldsymbol{\theta}_2\right)J_1(k_b|\mathbf{x}-\mathbf{z}|) \\ \vdots \\ e^{ik_b\boldsymbol{\theta}_N\cdot\mathbf{z}}\left(\frac{\mathbf{x}-\mathbf{z}}{|\mathbf{x}-\mathbf{z}|}\cdot\boldsymbol{\theta}_N\right)J_1(k_b|\mathbf{x}-\mathbf{z}|) \end{bmatrix}.$$

Now, let us write

$$|\mathbb{P}_{\text{noise}}(\mathbf{f}_\varepsilon(\mathbf{x},N))| = \left(\mathbb{P}_{\text{noise}}(\mathbf{f}_\varepsilon(\mathbf{x},N))\cdot\overline{\mathbb{P}_{\text{noise}}(\mathbf{f}_\varepsilon(\mathbf{x},N))}\right)^{1/2}$$

$$= \left(\sum_{n=1}^{N}\left(\frac{(1-C_\mu)^2}{N}+(\Psi_3(\mathbf{x},n)+\overline{\Psi_3(\mathbf{x},n)})+\Psi_4(\mathbf{x},n)\overline{\Psi_4(\mathbf{x},n)}\right)\right)^{1/2},$$

where

$$\Psi_3(\mathbf{x},n) = i(1-C_\mu)C_\mu\left(\frac{N}{2}-2\right)e^{ik_b\boldsymbol{\theta}_n\cdot(\mathbf{x}-\mathbf{z})}\left(\frac{\mathbf{x}-\mathbf{z}}{|\mathbf{x}-\mathbf{z}|}\cdot\boldsymbol{\theta}_n\right)J_1(k_b|\mathbf{x}-\mathbf{z}|),$$

$$\Psi_4(\mathbf{x},n) = -iC_\mu\left(\frac{N}{2}-2\right)\sqrt{N}e^{ik_b\boldsymbol{\theta}_n\cdot\mathbf{z}}\left(\frac{\mathbf{x}-\mathbf{z}}{|\mathbf{x}-\mathbf{z}|}\cdot\boldsymbol{\theta}_n\right)J_1(k_b|\mathbf{x}-\mathbf{z}|).$$

Applying (4.9), we can examine that

$$\sum_{n=1}^{N}\left(\frac{\mathbf{x}-\mathbf{z}}{|\mathbf{x}-\mathbf{z}|}\cdot\boldsymbol{\theta}_n\right)e^{ik_{\mathrm{b}}\boldsymbol{\theta}_n\cdot(\mathbf{x}-\mathbf{z})}\approx iN\left(\frac{\mathbf{x}-\mathbf{z}}{|\mathbf{x}-\mathbf{z}|}\cdot\frac{\mathbf{x}-\mathbf{z}}{|\mathbf{x}-\mathbf{z}|}\right)J_1(k_{\mathrm{b}}|\mathbf{x}-\mathbf{z}|)=J_1(k_{\mathrm{b}}|\mathbf{x}-\mathbf{z}|).$$

Hence,

$$\sum_{n=1}^{N}(\Psi_3(\mathbf{x},n)+\overline{\Psi_3(\mathbf{x},n)})\approx -2N(1-C_\mu)C_\mu\left(\frac{N}{2}-2\right)J_1(k_{\mathrm{b}}|\mathbf{x}-\mathbf{z}|)^2.$$

Now, applying (4.9) again, we can examine that

$$\begin{aligned}\sum_{n=1}^{N}\Psi_4(\mathbf{x},n)\overline{\Psi_4(\mathbf{x},n)}&\approx C_\mu^2\left(\frac{N}{2}-2\right)^2NJ_1(k_{\mathrm{b}}|\mathbf{x}-\mathbf{z}|)^2\sum_{n=1}^{N}\left(\frac{\mathbf{x}-\mathbf{z}}{|\mathbf{x}-\mathbf{z}|}\cdot\boldsymbol{\theta}_n\right)^2\\&=\frac{N^2}{2}C_\mu^2\left(\frac{N}{2}-2\right)^2J_1(k_{\mathrm{b}}|\mathbf{x}-\mathbf{z}|)^2.\end{aligned}$$

Therefore,

$$\begin{aligned}&|\mathbb{P}_{\mathrm{noise}}(\mathbf{f}_\varepsilon(\mathbf{x},N))|\\&\approx\left((1-C_\mu)^2-2N(1-C_\mu)C_\mu\left(\frac{N}{2}-2\right)J_1(k_{\mathrm{b}}|\mathbf{x}-\mathbf{z}|)^2+\frac{N^2}{2}C_\mu^2\left(\frac{N}{2}-2\right)^2J_1(k_{\mathrm{b}}|\mathbf{x}-\mathbf{z}|)^2\right)^{1/2}.\end{aligned}$$

Next, we consider the structure of $\mathbb{P}_{\mathrm{noise}}(\mathbf{f}_\mu(\mathbf{x},N))$. For the sake, let us denote

$$\Lambda(\mathbf{x},\mathbf{z})=J_0(k_{\mathrm{b}}|\mathbf{x}-\mathbf{z}|)+J_2(k_{\mathrm{b}}|\mathbf{x}-\mathbf{z}|)\quad\text{and}\quad\Gamma(\boldsymbol{\theta},\boldsymbol{\xi})=\left(\frac{\mathbf{x}-\mathbf{z}}{|\mathbf{x}-\mathbf{z}|}\cdot\boldsymbol{\theta}\right)\left(\frac{\mathbf{x}-\mathbf{z}}{|\mathbf{x}-\mathbf{z}|}\cdot\boldsymbol{\xi}\right).$$

Then based on (4.9),

$$\begin{bmatrix}(\boldsymbol{\theta}_1\cdot\boldsymbol{\theta}_1)e^{ik_{\mathrm{b}}(\boldsymbol{\theta}_1-\boldsymbol{\theta}_1)\cdot\mathbf{z}} & (\boldsymbol{\theta}_1\cdot\boldsymbol{\theta}_2)e^{ik_{\mathrm{b}}(\boldsymbol{\theta}_1-\boldsymbol{\theta}_2)\cdot\mathbf{z}} & \cdots & (\boldsymbol{\theta}_1\cdot\boldsymbol{\theta}_N)e^{ik_{\mathrm{b}}(\boldsymbol{\theta}_1-\boldsymbol{\theta}_N)\cdot\mathbf{z}}\\(\boldsymbol{\theta}_2\cdot\boldsymbol{\theta}_1)e^{ik_{\mathrm{b}}(\boldsymbol{\theta}_2-\boldsymbol{\theta}_1)\cdot\mathbf{z}} & (\boldsymbol{\theta}_2\cdot\boldsymbol{\theta}_2)e^{ik_{\mathrm{b}}(\boldsymbol{\theta}_2-\boldsymbol{\theta}_2)\cdot\mathbf{z}} & \cdots & (\boldsymbol{\theta}_2\cdot\boldsymbol{\theta}_N)e^{ik_{\mathrm{b}}(\boldsymbol{\theta}_2-\boldsymbol{\theta}_N)\cdot\mathbf{z}}\\\vdots & \vdots & \ddots & \vdots\\(\boldsymbol{\theta}_N\cdot\boldsymbol{\theta}_1)e^{ik_{\mathrm{b}}(\boldsymbol{\theta}_N-\boldsymbol{\theta}_1)\cdot\mathbf{z}} & (\boldsymbol{\theta}_N\cdot\boldsymbol{\theta}_2)e^{ik_{\mathrm{b}}(\boldsymbol{\theta}_N-\boldsymbol{\theta}_2)\cdot\mathbf{z}} & \cdots & (\boldsymbol{\theta}_N\cdot\boldsymbol{\theta}_N)e^{ik_{\mathrm{b}}(\boldsymbol{\theta}_N-\boldsymbol{\theta}_N)\cdot\mathbf{z}}\end{bmatrix}\begin{bmatrix}(\boldsymbol{\theta}_1\cdot\boldsymbol{\xi})e^{ik_{\mathrm{b}}\boldsymbol{\theta}_1\cdot\mathbf{x}}\\(\boldsymbol{\theta}_2\cdot\boldsymbol{\xi})e^{ik_{\mathrm{b}}\boldsymbol{\theta}_2\cdot\mathbf{x}}\\\vdots\\(\boldsymbol{\theta}_N\cdot\boldsymbol{\xi})e^{ik_{\mathrm{b}}\boldsymbol{\theta}_N\cdot\mathbf{x}}\end{bmatrix}$$

$$
\begin{aligned}
&= \begin{bmatrix} e^{ik_b\boldsymbol{\theta}_1\cdot\mathbf{z}}\sum_{n=1}^{N}(\boldsymbol{\theta}_1\cdot\boldsymbol{\theta}_n)(\boldsymbol{\xi}\cdot\boldsymbol{\theta}_n)e^{ik_b\boldsymbol{\theta}_n\cdot(\mathbf{x}-\mathbf{z})} \\ e^{ik_b\boldsymbol{\theta}_2\cdot\mathbf{z}}\sum_{n=1}^{N}(\boldsymbol{\theta}_2\cdot\boldsymbol{\theta}_n)(\boldsymbol{\xi}\cdot\boldsymbol{\theta}_n)e^{ik_b\boldsymbol{\theta}_n\cdot(\mathbf{x}-\mathbf{z})} \\ \vdots \\ e^{ik_b\boldsymbol{\theta}_N\cdot\mathbf{z}}\sum_{n=1}^{N}(\boldsymbol{\theta}_N\cdot\boldsymbol{\theta}_n)(\boldsymbol{\xi}\cdot\boldsymbol{\theta}_n)e^{ik_b\boldsymbol{\theta}_n\cdot(\mathbf{x}-\mathbf{z})} \end{bmatrix} \\
&\approx \begin{bmatrix} e^{ik_b\boldsymbol{\theta}_1\cdot\mathbf{z}}\left(\frac{N}{2}(\boldsymbol{\theta}_1\cdot\boldsymbol{\xi})\Lambda(\mathbf{x},\mathbf{z})-N\Gamma(\boldsymbol{\theta}_1,\boldsymbol{\xi})J_2(k_b|\mathbf{x}-\mathbf{z}|)\right) \\ e^{ik_b\boldsymbol{\theta}_2\cdot\mathbf{z}}\left(\frac{N}{2}(\boldsymbol{\theta}_2\cdot\boldsymbol{\xi})\Lambda(\mathbf{x},\mathbf{z})-N\Gamma(\boldsymbol{\theta}_2,\boldsymbol{\xi})J_2(k_b|\mathbf{x}-\mathbf{z}|)\right) \\ \vdots \\ e^{ik_b\boldsymbol{\theta}_N\cdot\mathbf{z}}\left(\frac{N}{2}(\boldsymbol{\theta}_N\cdot\boldsymbol{\xi})\Lambda(\mathbf{x},\mathbf{z})-N\Gamma(\boldsymbol{\theta}_N,\boldsymbol{\xi})J_2(k_b|\mathbf{x}-\mathbf{z}|)\right) \end{bmatrix}.
\end{aligned}
$$

Thus, we can examine that

$$
\begin{aligned}
\mathbb{P}_{\text{noise}}(\mathbf{f}_\mu(\mathbf{x},N)) &= \left(\mathbb{I}-\sum_{m=1}^{2}\mathbf{U}_m\mathbf{U}_m^*\right)\mathbf{f}_\mu(\mathbf{x},N) \approx \sqrt{\frac{2}{N}}(1-C_\mu)\begin{bmatrix}(\boldsymbol{\theta}_1\cdot\boldsymbol{\xi})e^{ik_b\boldsymbol{\theta}_1\cdot\mathbf{x}} \\ (\boldsymbol{\theta}_2\cdot\boldsymbol{\xi})e^{ik_b\boldsymbol{\theta}_2\cdot\mathbf{x}} \\ \vdots \\ (\boldsymbol{\theta}_N\cdot\boldsymbol{\xi})e^{ik_b\boldsymbol{\theta}_N\cdot\mathbf{x}}\end{bmatrix} \\
&\quad -\sqrt{2N}\left(\frac{N}{2}-2\right)C_\mu\begin{bmatrix} e^{ik_b\boldsymbol{\theta}_1\cdot\mathbf{z}}\left(\frac{(\boldsymbol{\theta}_1\cdot\boldsymbol{\xi})}{2}\Lambda(\mathbf{x},\mathbf{z})-\Gamma(\boldsymbol{\theta}_1,\boldsymbol{\xi})J_2(k_b|\mathbf{x}-\mathbf{z}|)\right) \\ e^{ik_b\boldsymbol{\theta}_2\cdot\mathbf{z}}\left(\frac{(\boldsymbol{\theta}_2\cdot\boldsymbol{\xi})}{2}\Lambda(\mathbf{x},\mathbf{z})-\Gamma(\boldsymbol{\theta}_2,\boldsymbol{\xi})J_2(k_b|\mathbf{x}-\mathbf{z}|)\right) \\ \vdots \\ e^{ik_b\boldsymbol{\theta}_N\cdot\mathbf{z}}\left(\frac{(\boldsymbol{\theta}_N\cdot\boldsymbol{\xi})}{2}\Lambda(\mathbf{x},\mathbf{z})-\Gamma(\boldsymbol{\theta}_N,\boldsymbol{\xi})J_2(k_b|\mathbf{x}-\mathbf{z}|)\right)\end{bmatrix}.
\end{aligned}
$$

Now, let us write

$$
\begin{aligned}
|\mathbb{P}_{\text{noise}}(\mathbf{f}_\mu(\mathbf{x},N))| &= \left(\mathbb{P}_{\text{noise}}(\mathbf{f}_\mu(\mathbf{x},N))\cdot\overline{\mathbb{P}_{\text{noise}}(\mathbf{f}_\mu(\mathbf{x},N))}\right)^{1/2} \\
&= \left(\sum_{n=1}^{N}\left(\frac{(1-C_\mu)^2}{N}+(\Psi_5(\mathbf{x},n)+\overline{\Psi_5(\mathbf{x},n)})+\Psi_6(\mathbf{x},n)\overline{\Psi_6(\mathbf{x},n)}\right)\right)^{1/2},
\end{aligned}
$$

where

$$\Psi_5(\mathbf{x},n)\approx -2(1-C_\mu)C_\mu\left(\frac{N}{2}-2\right)(\boldsymbol{\theta}_n\cdot\boldsymbol{\xi})e^{ik_{\rm b}\boldsymbol{\theta}_n\cdot(\mathbf{x}-\mathbf{z})}\left(\frac{(\boldsymbol{\theta}_n\cdot\boldsymbol{\xi})}{2}\Lambda(\mathbf{x},\mathbf{z})-\Gamma(\boldsymbol{\theta}_n,\boldsymbol{\xi})J_2(k_{\rm b}|\mathbf{x}-\mathbf{z}|)\right),$$

$$\Psi_6(\mathbf{x},n)\approx\sqrt{2N}\left(\frac{N}{2}-2\right)C_\mu e^{ik_{\rm b}\boldsymbol{\theta}_n\cdot\mathbf{z}}\left(\frac{(\boldsymbol{\theta}_n\cdot\boldsymbol{\xi})}{2}\Lambda(\mathbf{x},\mathbf{z})-\Gamma(\boldsymbol{\theta}_n,\boldsymbol{\xi})J_2(k_{\rm b}|\mathbf{x}-\mathbf{z}|)\right).$$

Now, applying (4.9), we can evaluate

$$\begin{aligned}&\sum_{n=1}^{N}(\Psi_5(\mathbf{x},n)+\overline{\Psi_5(\mathbf{x},n)})\\ &\approx -2N(1-C_\mu)C_\mu\left(\frac{N}{2}-2\right)\\ &\quad\times\left(\frac{1}{4}\Lambda(\mathbf{x},\mathbf{z})^2-\Gamma(\boldsymbol{\xi},\boldsymbol{\xi})\Lambda(\mathbf{x},\mathbf{z})J_2(k_{\rm b}|\mathbf{x}-\mathbf{z}|)+\Gamma(\boldsymbol{\xi},\boldsymbol{\xi})J_2(k_{\rm b}|\mathbf{x}-\mathbf{z}|)^2\right)\end{aligned}$$

and

$$\begin{aligned}&\sum_{n=1}^{N}(\Psi_6(\mathbf{x},n)\overline{\Psi_6(\mathbf{x},n)})\\ &\approx 2N\left(\frac{N}{2}-2\right)^2C_\mu^2\sum_{n=1}^{N}\left(\frac{(\boldsymbol{\theta}_n\cdot\boldsymbol{\xi})^2}{4}\Lambda(\mathbf{x},\mathbf{z})^2-(\boldsymbol{\theta}_n\cdot\boldsymbol{\xi})\Gamma(\boldsymbol{\theta}_n,\boldsymbol{\xi})\Lambda(\mathbf{x},\mathbf{z})J_2(k_{\rm b}|\mathbf{x}-\mathbf{z}|)\right.\\ &\qquad\left.+\Gamma(\boldsymbol{\xi},\boldsymbol{\xi})^2J_2(k_{\rm b}|\mathbf{x}-\mathbf{z}|)^2\right)\\ &=N^2\left(\frac{N}{2}-2\right)^2C_\mu^2\left(\frac{1}{4}\Lambda(\mathbf{x},\mathbf{z})^2-\Gamma(\boldsymbol{\xi},\boldsymbol{\xi})\Lambda(\mathbf{x},\mathbf{z})J_2(k_{\rm b}|\mathbf{x}-\mathbf{z}|)+\Gamma(\boldsymbol{\xi},\boldsymbol{\xi})J_2(k_{\rm b}|\mathbf{x}-\mathbf{z}|)^2\right).\end{aligned}$$

Therefore,

$$\begin{aligned}&|\mathbb{P}_{\rm noise}(\mathbf{f}_\mu(\mathbf{x},N))|\\ &\approx\left((1-C_\mu)^2-2N(1-C_\mu)C_\mu\left(\frac{N}{2}-2\right)\Psi(\mathbf{x},\mathbf{z})+N^2\left(\frac{N}{2}-2\right)^2C_\mu^2\Psi(\mathbf{x},\mathbf{z})\right)^{1/2}.\end{aligned}$$

With this, we can derive the structure (4.11). □

Based on the identified structures (4.10) and (4.11), we can observe several properties of the imaging functions.

Remark 4.5 (Applicability of MUSIC)**.** The imaging function $\mathfrak{F}_{\rm DE}^{(\varepsilon)}(\mathbf{x},N)$ consists of $J_1(k_{\rm b}|\mathbf{x}-\mathbf{z}|)$. Therefore, as in traditional MUSIC-type imaging, the map of $\mathfrak{F}_{\rm DE}^{(\varepsilon)}(\mathbf{x},N)$ will contain two peaks of large large magnitude in the neighborhood of D and many artifacts with small magnitude. In contrast, since $\mathfrak{F}_{\rm DE}^{(\mu)}(\mathbf{x},N)$ consists of both $J_0(k_{\rm b}|\mathbf{x}-\mathbf{z}|)$ and $J_2(k_{\rm b}|\mathbf{x}-\mathbf{z}|)$, the map of $\mathfrak{F}_{\rm DE}^{(\mu)}(\mathbf{x},N)$ will contain peak of large magnitude at $\mathbf{z}=\mathbf{x}\in D$.

Remark 4.6 (Influence of total number of incident/observation directions)**.** Following [38, Section 3.5], $\mathfrak{F}_{\mathrm{TE}}^{(\mu)}(\mathbf{x},N)$ satisfies

$$\lim_{N\to\infty}\mathfrak{F}_{\mathrm{TE}}^{(\mu)}(\mathbf{x},N)=\Big(1-J_1(k_{\mathrm{b}}|\mathbf{x}-\mathbf{z}|)^2\Big)^{-1/2}.$$

Therefore, similar to TM polarization, the obtained result should be poorer than the result obtained via $\mathfrak{F}_{\mathrm{TE}}^{(\mu)}(\mathbf{x},N)$ i.e., a result of poor resolution will be obtained if N is small.

Remark 4.7. Unlike Theorem 4.1, the complete form of C_μ in (4.10) is unknown. To examine an approximate form of C_μ, we follow a process similar to that in Remark 4.4. Since

$$\lim_{N\to\infty}\mathfrak{F}_{\mathrm{DE}}^{(\varepsilon)}(\mathbf{x},N)=\lim_{N\to\infty}\mathfrak{F}_{\mathrm{TE}}^{(\mu)}(\mathbf{x},N),$$

it can be said that

$$\begin{aligned}&\lim_{N\to\infty}\left[(1-C_\mu)^2-2N(1-C_\mu)C_\mu\left(\frac{N}{2}-2\right)J_1(k_{\mathrm{b}}|\mathbf{x}-\mathbf{z}|)^2+\frac{N^2}{2}C_\mu^2\left(\frac{N}{2}-2\right)^2J_1(k_{\mathrm{b}}|\mathbf{x}-\mathbf{z}|)^2\right]\\&=1-J_1(k_{\mathrm{b}}|\mathbf{x}-\mathbf{z}|)^2.\end{aligned}$$

Hence, similar to the TM polarization case, we can examine that $C_\mu=\mathcal{O}(N^{-2})$. Notice that if C_μ satisfies

$$N\left(\frac{N}{2}-2\right)C_\mu=(2+\sqrt{2})(1-C_\mu)\quad\text{or equivalently}\quad C_\mu=\frac{4+2\sqrt{2}}{N^2-4N+4+2\sqrt{2}}=\mathcal{O}\left(\frac{1}{N^2}\right),$$

then similar to the TM polarization case, $\mathfrak{F}_{\mathrm{DE}}^{(\varepsilon)}(\mathbf{x},N)$ can be written as

$$\mathfrak{F}_{\mathrm{DE}}^{(\varepsilon)}(\mathbf{x},N)=\frac{1}{1-C_\mu}\Big(1-J_1(k_{\mathrm{b}}|\mathbf{x}-\mathbf{z}|)^2\Big)^{-1/2}=\left(\frac{N^2-4N+4+2\sqrt{2}}{N^2-4N}\right)\Big(1-J_1(k_{\mathrm{b}}|\mathbf{x}-\mathbf{z}|)^2\Big)^{-1/2}.$$

Remark 4.8. Same as the Remark 4.7, if C_μ of (4.11) satisfies

$$N\left(\frac{N}{2}-2\right)C_\mu=(1-C_\mu)\quad\text{or equivalently}\quad C_\mu=\frac{2}{N^2-4N+2}=\mathcal{O}\left(\frac{1}{N^2}\right),$$

then $\mathfrak{F}_{\mathrm{DE}}^{(\mu)}(\mathbf{x},N)$ can be written as

$$\mathfrak{F}_{\mathrm{DE}}^{(\mu)}(\mathbf{x},N)=\frac{1}{1-C_\mu}\Big(1-\Psi(\mathbf{x},\mathbf{z})\Big)^{-1/2}=\left(\frac{N^2-4N+2}{N^2-4N}\right)\Big(1-\Psi(\mathbf{x},\mathbf{z})\Big)^{-1/2}.$$

Remark 4.9. Opposite to the Corollary 4.1, the unique determination in TE polarization cannot be guaranteed via the maps of $\mathfrak{F}_{\mathrm{DE}}^{(\varepsilon)}(\mathbf{x},N)$ and $\mathfrak{F}_{\mathrm{DE}}^{(\mu)}(\mathbf{x},N)$. Fortunately, throughout simulation results in Section 5, small objects can be uniquely identified through the map of $\mathfrak{F}_{\mathrm{DE}}^{(\mu)}(\mathbf{x},N)$ for sufficiently large N and a proper selection of $\boldsymbol{\zeta}$ in (3.7).

5 Simulation results with synthetic and experimental data

In order to validate the results in Theorems 4.1 and 4.2, some results of numerical simulation are exhibited. Motivated by the simulation configuration [14], we set the far-field pattern data were obtained in the anechoic chamber with vacuum permittivity $\varepsilon_{\rm b} = 8.854\times10^{-12}\,{\rm F/m}$ and permeability $\mu_{\rm b} = 1.257\times10^{-6}\,{\rm H/m}$. The ROI Ω was selected as a square region $(-0.1{\rm m},0.1{\rm m})\times(-0.1{\rm m},0.1{\rm m})$ and three circular objects $D_m \subset \Omega$, $m = 1,2,3$, with same radii $\alpha_m = 0.01{\rm m}$, permittivities ε_m, permeabilities μ_m, and locations $\mathbf{z}_1 = (0.07{\rm m},0.05{\rm m})$, $\mathbf{z}_2 = (-0.07{\rm m},0.00{\rm m})$, and $\mathbf{z}_3 = (0.02{\rm m},-0.05{\rm m})$ were chosen. With this configuration, the far-field pattern data $u_\infty(\boldsymbol{\vartheta}_j,\boldsymbol{\theta}_l)$ of $\mathbb{K}$ were generated by solving the Folly-Lax formulation (see [23] for instance). After the generation of the far-field pattern, 20dB white Gaussian random noise was added to the unperturbed data.

Example 5.1 (Dielectric permittivity contrast case)**.** Fig. 2 shows the maps of $\mathfrak{F}_{\rm TM}(\mathbf{x},N)$ and $\mathfrak{F}_{\rm DM}(\mathbf{x},N)$ with $f=1$GHz for $N=12$ and $N=36$ directions when $\varepsilon_m=5\varepsilon_{\rm b}$ and $\mu_m\equiv\mu_{\rm b}$. Based on this result, the existence of three objects D_m can be recognized through the maps of $\mathfrak{F}_{\rm TM}(\mathbf{x},N)$ and $\mathfrak{F}_{\rm DM}(\mathbf{x},N)$ but retrieved location of D_3 through the map of $\mathfrak{F}_{\rm DM}(\mathbf{x},N)$ is not accurate.

Fig. 3 shows the maps of $\mathfrak{F}_{\rm TM}(\mathbf{x},N)$ and $\mathfrak{F}_{\rm DM}(\mathbf{x},N)$ with $f=2$GHz for $N=12$ and $N=36$ directions. Opposite to the imaging result at $f=1$GHz, it is possible to retrieve the location of every objects very accurately through the map of $\mathfrak{F}_{\rm DM}(\mathbf{x},N)$. However, although retrieved location of D_3 with $N=36$ is more accurate than the one with $N=12$,

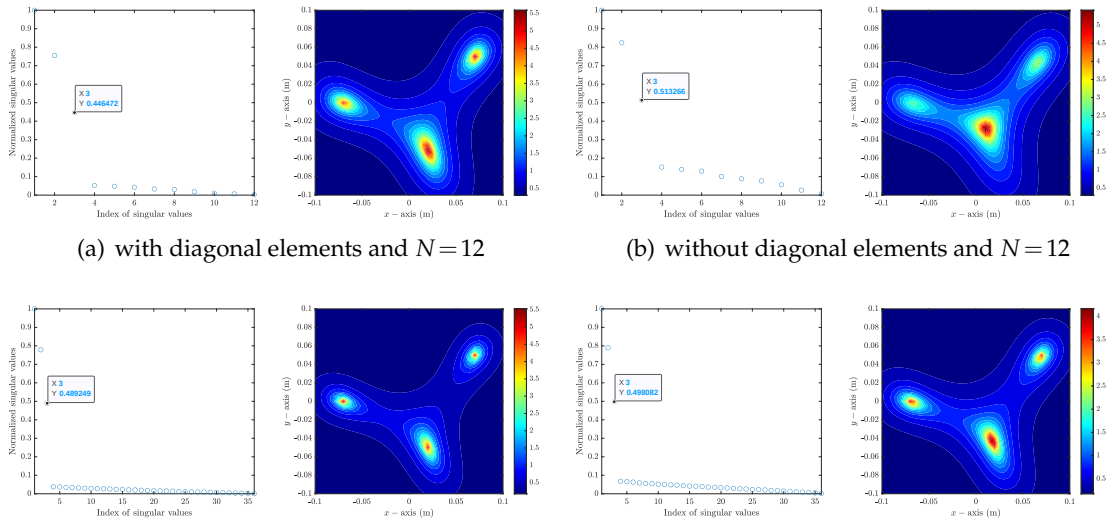

(a) with diagonal elements and $N=12$

(b) without diagonal elements and $N=12$

(c) with diagonal elements and $N=36$

(d) without diagonal elements and $N=36$

Figure 2: (Example 5.1) Distribution of normalized singular values and maps of $\mathfrak{F}_{\rm TM}(\mathbf{x},N)$ and $\mathfrak{F}_{\rm DM}(\mathbf{x},N)$ at $f=1$GHz.

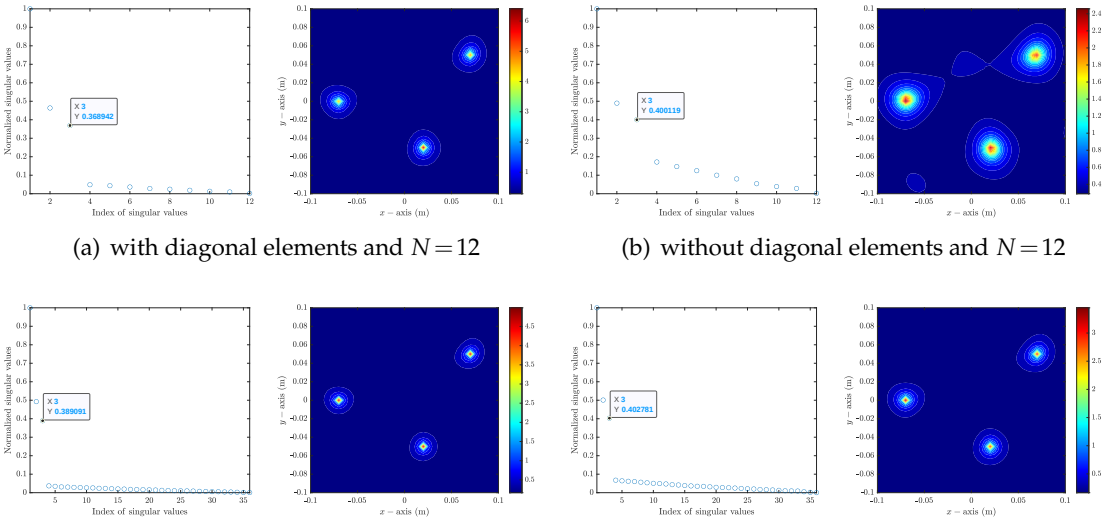

(a) with diagonal elements and $N=12$ (b) without diagonal elements and $N=12$

(c) with diagonal elements and $N=36$ (d) without diagonal elements and $N=36$

Figure 3: (Example 5.1) Distribution of normalized singular values and maps of $\mathfrak{F}_{\mathrm{TM}}(\mathbf{x},N)$ and $\mathfrak{F}_{\mathrm{DM}}(\mathbf{x},N)$ at $f=2$GHz.

exact location of D_3 cannot be retrieved still.

Based on the simulation results, we can conclude that it will be very difficult to identify exact location of objects without diagonal elements of MSR matrix when total number of directions N is small. This is the reason why the condition of sufficiently large N is needed in Theorem 4.1.

Example 5.2 (Magnetic permeability contrast case)**.** Fig. 4 shows the maps of $\mathfrak{F}^{(\varepsilon)}_{\mathrm{TE}}(\mathbf{x},N)$ and $\mathfrak{F}^{(\varepsilon)}_{\mathrm{DE}}(\mathbf{x},N)$ with $f=2$GHz for $N=12$ and $N=36$ directions when $\varepsilon_m\equiv\varepsilon_{\mathrm{b}}$ and $\mu_m=5\mu_{\mathrm{b}}$. Opposite to the Example 5.1, it is impossible to recognize the existence of objects with and without diagonal elements of the MSR matrix.

Based on the simulation result with $f=4$GHz with $N=12$ directions, it is still impossible to retrieve the objects through the maps of $\mathfrak{F}^{(\varepsilon)}_{\mathrm{TE}}(\mathbf{x},N)$ and $\mathfrak{F}^{(\varepsilon)}_{\mathrm{DE}}(\mathbf{x},N)$. Moreover, it is very difficult to discriminate nonzero singular values of the MSR matrix without diagonal elements, refer to Fig. 5. Fortunately, by increasing total number of directions $N=36$, it is very easy to discriminate nonzero singular values and possible to identify the existence of objects by regarding the rings in the neighborhood of all $\mathbf{z}_m\in D_m$. This result supports the Remark 4.5 and we conclude that not only large number of directions N but also high frequency f must be applied to guarantee good imaging results.

Example 5.3 (Magnetic permeability contrast case)**.** Fig. 5 shows the maps of $\mathfrak{F}^{(\mu)}_{\mathrm{TE}}(\mathbf{x},N)$ and $\mathfrak{F}^{(\mu)}_{\mathrm{DE}}(\mathbf{x},N)$ with $\boldsymbol{\xi}=(0,1)$ and $f=2$GHz for $N=12$ and $N=36$ directions when $\varepsilon_m\equiv\varepsilon_{\mathrm{b}}$

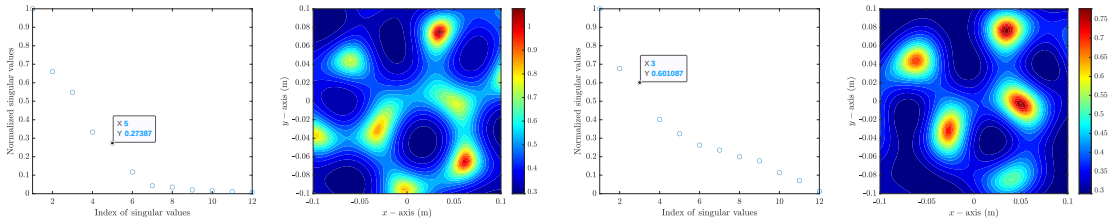

(a) with diagonal elements and $N=12$ (b) without diagonal elements and $N=12$

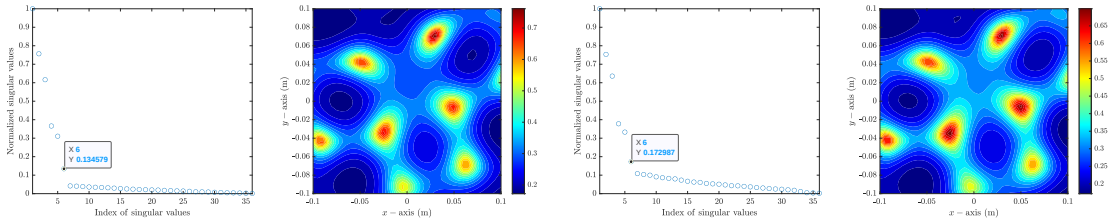

(c) with diagonal elements and $N=36$ (d) without diagonal elements and $N=36$

Figure 4: (Example 5.2) Distribution of normalized singular values and maps of $\mathfrak{F}_{\mathrm{TE}}^{(\varepsilon)}(\mathbf{x},N)$ and $\mathfrak{F}_{\mathrm{DE}}^{(\varepsilon)}(\mathbf{x},N)$ at $f=2$GHz.

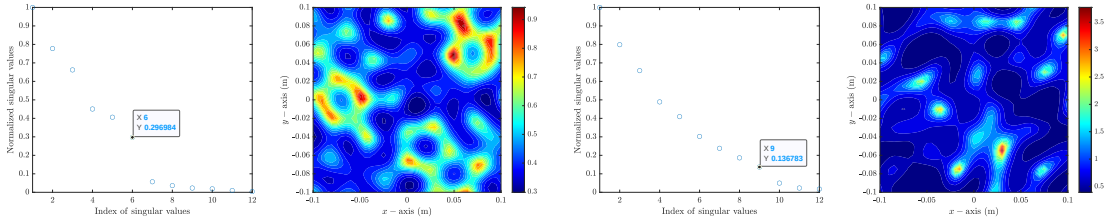

(a) with diagonal elements and $N=12$ (b) without diagonal elements and $N=12$

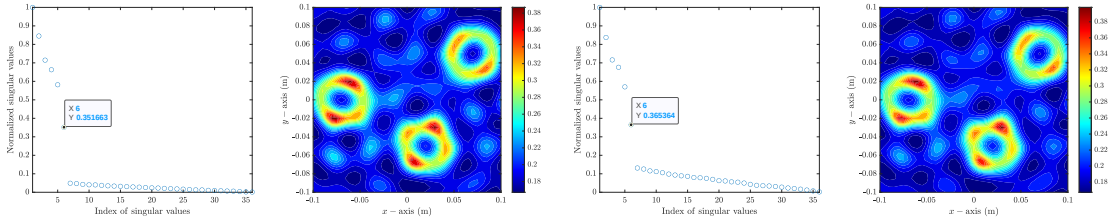

(c) with diagonal elements and $N=36$ (d) without diagonal elements and $N=36$

Figure 5: (Example 5.2) Distribution of normalized singular values and maps of $\mathfrak{F}_{\mathrm{TE}}^{(\varepsilon)}(\mathbf{x},N)$ and $\mathfrak{F}_{\mathrm{DE}}^{(\varepsilon)}(\mathbf{x},N)$ at $f=4$GHz.

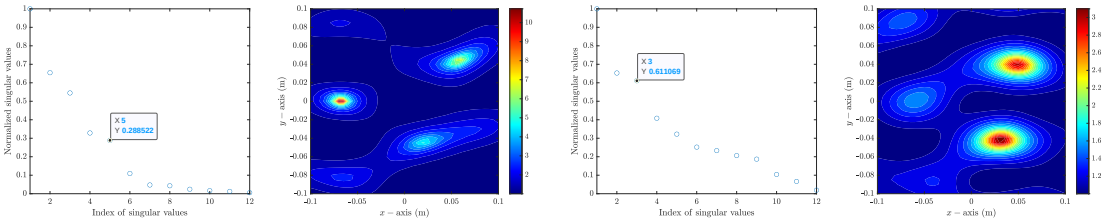

(a) with diagonal elements and $N=12$ (b) without diagonal elements and $N=12$

(c) with diagonal elements and $N=36$ (d) without diagonal elements and $N=36$

Figure 6: (Example 5.3) Distribution of normalized singular values and maps of $\mathfrak{F}^{(\mu)}_{\mathrm{TE}}(\mathbf{x},N)$ and $\mathfrak{F}^{(\mu)}_{\mathrm{DE}}(\mathbf{x},N)$ at $f=2$GHz.

and $\mu_m=5\mu_{\mathrm{b}}$. Opposite to the Example 5.2, it is impossible to recognize the existence and location of objects with and without diagonal elements of the MSR matrix for $N=36$. Unfortunately, if $N=12$ and the diagonal elements of the MSR matrix was missing, some objects cannot be recognized because the magnitude at the such objects is very small.

Based on the simulation result with $\boldsymbol{\xi}=(0,1)$ and $f=4$GHz for $N=12$ and 36 directions, unlike to the Example 5.2, it is impossible to recognize the objects through the maps of $\mathfrak{F}^{(\mu)}_{\mathrm{TE}}(\mathbf{x},N)$ and $\mathfrak{F}^{(\mu)}_{\mathrm{DE}}(\mathbf{x},N)$. It is interesting to examine that unlike to the case $N=12$, it is very difficult to discriminate nonzero singular values of the MSR matrix without diagonal elements and imaging result of $\mathfrak{F}^{(\mu)}_{\mathrm{DE}}(\mathbf{x},N)$ is very poor. Fortunately, by adopting $N=36$ directions, it is very easy to select nonzero singular values and possible to retrieve all objects.

Example 5.4 (Simulation results with experimental data)**.** Here, we let us consider the simulation results with experimental data [14]. Following to the simulation configuration in the presence of two dielectric objects (`twodielTM_8f.exp`), the range of receivers is restricted from 60° to 300°, with a step size of 5° based on each direction of the transmitters. The transmitters are evenly distributed with step sizes of 10° from 0° to 350°. As a result, many elements (totally, 36×23 measurement data) including the diagonal of the matrix $\mathbb{K}\in\mathbb{C}^{36\times72}$ cannot be measured, We refer to Fig. 8.

Although, the range of the $\mathbb{K}$ is unknown, we consider the application of the MUSIC.

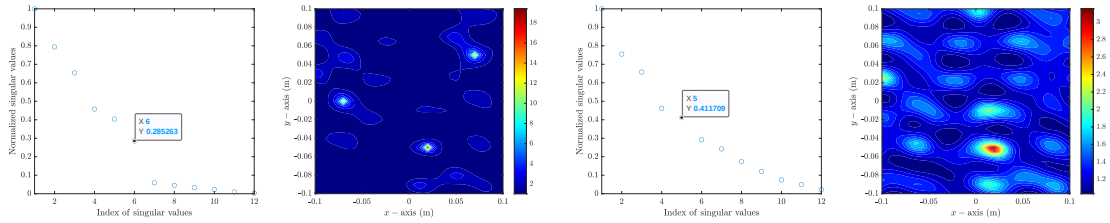

(a) with diagonal elements and $N=12$ (b) without diagonal elements and $N=12$

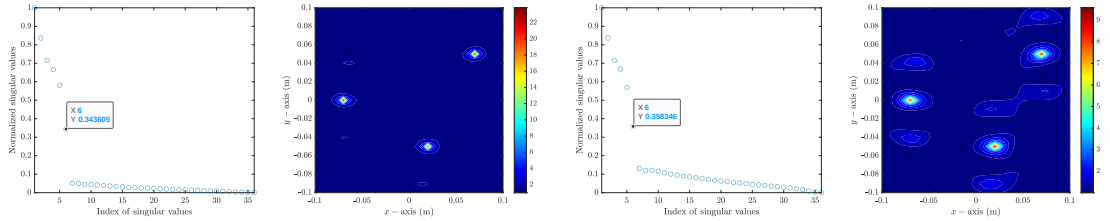

(c) with diagonal elements and $N=36$ (d) without diagonal elements and $N=36$

Figure 7: (Example 5.3) Distribution of normalized singular values and maps of $\mathfrak{F}_{\mathrm{TE}}^{(\mu)}(\mathbf{x},N)$ and $\mathfrak{F}_{\mathrm{DE}}^{(\mu)}(\mathbf{x},N)$ at $f=4$GHz.

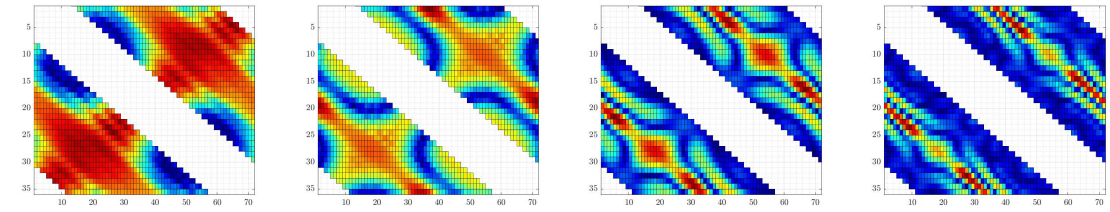

(a) $f=1$GHz (b) $f=2$GHz (c) $f=4$GHz (d) $f=6$GHz

Figure 8: (Example 5.4) Visualization of the absolute value of MSR matrix.

To this end, let us perform the SVD

$$\mathbb{K}=\sum_{n=1}^{N}\sigma_n\mathbf{U}_n\mathbf{V}_n^*\approx\sum_{n=1}^{N'}\sigma_n\mathbf{U}_n\mathbf{V}_n^*.$$

Since $\mathbb{K}$ is non-symmetric, we cannot use the test vector $\mathbf{f}_\varepsilon(\mathbf{x},N)$ of (3.4) directly. Instead, based on the recent studies [44, 45], we generate projection operators onto the noise subspaces

$$\mathbb{P}_{\mathrm{noise}}=\mathbb{I}_{36}-\sum_{n=1}^{N'}\mathbf{U}_n\mathbf{U}_n^* \quad\text{and}\quad \mathbb{Q}_{\mathrm{noise}}=\mathbb{I}_{72}-\sum_{n=1}^{N'}\mathbf{V}_n\mathbf{V}_n^*,$$

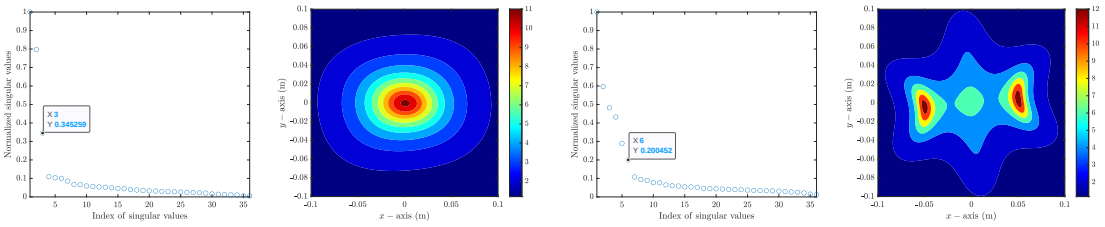

(a) $f=1$GHz (b) $f=2$GHz

(c) $f=4$GHz (d) $f=6$GHz

Figure 9: (Example 5.4) Distribution of normalized singular values and maps of $\mathfrak{F}_{\mathrm{DM}}(\mathbf{x},N)$.

and unit test vectors

$$\mathbf{f}(\mathbf{x})=\frac{1}{\sqrt{36}}\left(e^{ik_b\boldsymbol{\theta}_1\cdot\mathbf{x}},e^{ik_b\boldsymbol{\theta}_2\cdot\mathbf{x}},\ldots,e^{ik_b\boldsymbol{\theta}_{36}\cdot\mathbf{x}}\right)^T \text{ and } \mathbf{g}(\mathbf{x})=\frac{1}{\sqrt{72}}\left(e^{-ik_b\boldsymbol{\vartheta}_1\cdot\mathbf{x}},e^{-ik_b\boldsymbol{\vartheta}_2\cdot\mathbf{x}},\ldots,e^{-ik_b\boldsymbol{\vartheta}_{72}\cdot\mathbf{x}}\right)^T.$$

Then, the imaging function can be introduced as

$$\mathfrak{F}_{\mathrm{DM}}(\mathbf{x},N)=\frac{1}{2}\left(\frac{1}{|\mathbb{P}_{\mathrm{noise}}(\mathbf{f}(\mathbf{x}))|}+\frac{1}{|\mathbb{Q}_{\mathrm{noise}}(\mathbf{g}(\mathbf{x}))|}\right).$$

Based on the imaging results in Fig. 9, although exact shape of objects cannot be retrieved, the existence and outline shape of objects can be retrieved at $f=4$GHz and 6GHz. However, if one applies low frequency, it will be impossible to recognize the existence of objects (at $f=1$GHz) or very difficult to retrieve the outline shape of objects (at $f=2$GHz).

6 Conclusion

In this study, we considered the MUSIC algorithm for localizing two-dimensional small object modeled via TM and TE polarization when the diagonal elements of MSR matrix cannot be determined. We investigated a mathematical structure of the imaging functions by establishing a relationship with the Bessel function of order 0 (TM polarization), 1 (TE polarization), and both 0 and 2 (TE polarization). Based on the investigated structures,

we confirmed that MUSIC can be applied to retrieve location of small object without the diagonal elements of the MSR matrix in both TM and TE polarizations when total number of incident and observation directions is sufficiently large.

Unfortunately, exact expression of C_μ in Theorem 4.2 is still unknown. Derivation of exact structure of the imaging function in TE polarization will be an interesting research subject. In this study, the structures were derived in the presence of single object but MUSIC can be applied to the identification of multiple, small objects on the basis of simulation results. Extension to the multiple, small objects will be the forthcoming work. Finally, extension to the three-dimensional inverse scattering problem will be an interesting research topic.

Acknowledgments

The author would like to thank the anonymous reviewers for their valuable comments that help to increase the quality of the paper. This work was supported by the National Research Foundation of Korea (NRF) grant funded by the Korea government (MSIT) (NRF-2020R1A2C1A01005221).

References

[1] C. Y. Ahn, K. Jeon, and W.-K. Park, Analysis of MUSIC-type imaging functional for single, thin electromagnetic inhomogeneity in limited-view inverse scattering problem, J. Comput. Phys., 291 (2015), 198–217.
[2] C. J. S. Alves and P. Serranho, On the identification of the flatness of a sound-hard acoustic crack, Math. Comput. Simulat., 66 (2004), 337–353.
[3] H. Ammari, An Introduction to Mathematics of Emerging Biomedical Imaging, in Mathematics and Applications Series 62, Springer, Berlin, 2008.
[4] H. Ammari, J. Garnier, V. Jugnon, and H. Kang, Stability and resolution analysis for a topological derivative based imaging functional, SIAM J. Control. Optim., 50 (2012), 48–76.
[5] H. Ammari, J. Garnier, H. Kang, M. Lim, and K. Sølna, Multistatic imaging of extended targets, SIAM J. Imag. Sci., 5 (2012), 564–600.
[6] H. Ammari, J. Garnier, H. Kang, W.-K. Park, and K. Sølna, Imaging schemes for perfectly conducting cracks, SIAM J. Appl. Math., 71 (2011), 68–91.
[7] H. Ammari, E. Iakovleva, and D. Lesselier, A MUSIC algorithm for locating small inclusions buried in a half-space from the scattering amplitude at a fixed frequency, Multiscale Model. Sim., 3 (2005), 597–628.
[8] H. Ammari, E. Iakovleva, D. Lesselier, and G. Perrusson, MUSIC type electromagnetic imaging of a collection of small three-dimensional inclusions, SIAM J. Sci. Comput., 29 (2007), 674–709.
[9] H. Ammari and H. Kang, Reconstruction of Small Inhomogeneities from Boundary Measurements, in Lecture Notes in Mathematics 1846, Springer-Verlag, Berlin, 2004.
[10] H. Ammari, H. Kang, E. Kim, K. Louati, and M. Vogelius, A MUSIC-type algorithm for detecting internal corrosion from electrostatic boundary measurements, Numer. Math., 108 (2008), 501–528.

[11] H. Ammari, H. Kang, H. Lee, and W.-K. Park, Asymptotic imaging of perfectly conducting cracks, SIAM J. Sci. Comput., 32 (2010), 894–922.
[12] R. C. Aster, B. Borchers, and C. H. Thurber, Parameter Estimation and Inverse Problems, Elsevier, 2013.
[13] Q. Bao, S. Yuan, and F. Guo, A new synthesis aperture-MUSIC algorithm for damage diagnosis on complex aircraft structures, Mech. Syst. Signal Proc., 136 (2020), 106491.
[14] K. Belkebir and M. Saillard, Special section: Testing inversion algorithms against experimental data, Inverse Probl., 17 (2001), 1565–1571.
[15] N. Bleistein, J. Cohen, and J. S. Stockwell Jr, Mathematics of Multidimensional Seismic Imaging, Migration, and Inversion, in Interdisciplinary Applied Mathematics Series 13, Springer, New York, 2001.
[16] F. Cakoni and D. Colton, The linear sampling method for cracks, Inverse Probl., 19 (2003), 279–295.
[17] X. Chen and K. Agarwal, MUSIC algorithm for two-dimensional inverse problems with special characteristics of cylinders, IEEE Trans. Antennas Propag., 56 (2008), 1080–1812.
[18] M. Cherniakov, Bistatic Radar: Principles and Practice, Wiley, 2007.
[19] D. Colton and R. Kress, Inverse Acoustic and Electromagnetic Scattering Problems, in Mathematics and Applications Series 93, Springer, New York, 1998.
[20] F. Comblet, A. Khenchaf, A. Baussard, and F. Pellen, Bistatic synthetic aperture radar imaging: Theory, simulations, and validations, IEEE Trans. Antennas Propag., 54 (2006), 3529–3540.
[21] O. Dorn and D. Lesselier, Level set methods for inverse scattering, Inverse Probl., 22 (2006), R67–R131.
[22] S. Hou, K. Sølna, and H. Zhao, A direct imaging algorithm for extended targets, Inverse Probl., 22 (2006), 1151–1178.
[23] K. Huang, K. Sølna, and H. Zhao, Generalized Foldy-Lax formulation, J. Comput. Phys., 229 (2010), 4544–4553.
[24] E. Iakovleva, S. Gdoura, D. Lesselier, and G. Perrusson, Multi-static response matrix of a 3D inclusion in half space and MUSIC imaging, IEEE Trans. Antennas Propag., 55 (2007), 2598–2609.
[25] K. Ikeda, M. Yoshimi, and C. Miki, Electrical potential drop method for evaluating crack depth, Int. J. Fract., 47 (1991), 25–38.
[26] K. Ito, B. Jin, and J. Zou, A direct sampling method to an inverse medium scattering problem, Inverse Probl., 28 (2012), 025003.
[27] L. Jofre, A. Broquetas, J. Romeu, S. Blanch, A. P. Toda, X. Fabregas, and A. Cardama, UWB tomographic radar imaging of penetrable and impenetrable objects, Proc. IEEE, 97 (2009), 451–464.
[28] Y.-D. Joh, Y. M. Kwon, and W.-K. Park, MUSIC-type imaging of perfectly conducting cracks in limited-view inverse scattering problems, Appl. Math. Comput., 240 (2014), 273–280.
[29] S. Kang, M. Lim, and W.-K. Park, Fast identification of short, linear perfectly conducting cracks in the bistatic measurement configuration, J. Comput. Phys., 468 (2022), 111479.
[30] S. Kang and W.-K. Park, Application of MUSIC algorithm for a fast identification of small perfectly conducting cracks in limited-aperture inverse scattering problem, Comput. Math. Appl., 117 (2022), 97–112.
[31] A. Kirsch and N. Grinberg, The Factorization Method for Inverse Problems, Oxford University Press, 2008.
[32] A. Kirsch and S. Ritter, A linear sampling method for inverse scattering from an open arc,

Inverse Probl., 16 (2000), 89–105.
[33] R. Kress, Newton's method for inverse obstacle scattering meets the method of least squares, Inverse Probl., 19 (2003), S91–S104.
[34] K. H. Leem, J. Liu, and G. Pelekanos, An extended direct factorization method for inverse scattering with limited aperture data, Inverse Probl. Sci. Eng., 28 (2020), 754–776.
[35] N. K. Nikolova, Introduction to Microwave Imaging, Cambridge University Press, 2017.
[36] J. W. Odendaal, E. Barnard, and C. W. I. Pistorius, Two-dimensional superresolution radar imaging using the MUSIC algorithm, IEEE Trans. Antennas Propag., 42 (1994), 1386–1391.
[37] W.-K. Park, Topological derivative strategy for one-step iteration imaging of arbitrary shaped thin, curve-like electromagnetic inclusions, J. Comput. Phys., 231 (2012), 1426–1439.
[38] W.-K. Park, Asymptotic properties of MUSIC-type imaging in two-dimensional inverse scattering from thin electromagnetic inclusions, SIAM J. Appl. Math., 75 (2015), 209–228.
[39] W.-K. Park, Multi-frequency subspace migration for imaging of perfectly conducting, arc-like cracks in full- and limited-view inverse scattering problems, J. Comput. Phys., 283 (2015), 52–80.
[40] W.-K. Park, A novel study on subspace migration for imaging of a sound-hard arc, Comput. Math. Appl., 74 (2017), 3000–3007.
[41] W.-K. Park, Direct sampling method for retrieving small perfectly conducting cracks, J. Comput. Phys., 373 (2018), 648–661.
[42] W.-K. Park, Real-time microwave imaging of unknown anomalies via scattering matrix, Mech. Syst. Signal Proc., 118 (2019), 658–674.
[43] W.-K. Park, Application of MUSIC algorithm in real-world microwave imaging of unknown anomalies from scattering matrix, Mech. Syst. Signal Proc., 153 (2021), 107501.
[44] W.-K. Park, A novel study on the MUSIC-type imaging of small electromagnetic inhomogeneities in the limited-aperture inverse scattering problem, J. Comput. Phys., 460 (2022), 111191.
[45] W.-K. Park, Real-time detection of small anomaly from limited-aperture measurements in real-world microwave imaging, Mech. Syst. Signal Proc., 171 (2022), 108937.
[46] W.-K. Park, On the application of MUSIC algorithm for identifying short sound-hard arcs in limited-view inverse acoustic problem, Wave Motion, 117 92023), 103114.
[47] W.-K. Park and D. Lesselier, Electromagnetic MUSIC-type imaging of perfectly conducting, arc-like cracks at single frequency, J. Comput. Phys., 228 (2009), 8093–8111.
[48] W.-K. Park and D. Lesselier, Reconstruction of thin electromagnetic inclusions by a level set method, Inverse Probl., 25 (2009), 085010.
[49] T. Rao and X. Chen, Analysis of the time-reversal operator for a single cylinder under two-dimensional settings, J. Electromagn. Waves Appl., 20 (2006), 2153–2165.
[50] B. Scholz, Towards virtual electrical breast biopsy: Space frequency MUSIC for trans-admittance data, IEEE Trans. Med. Imag., 21 (2002), 588–595.
[51] S.-H. Son and W.-K. Park, Application of the bifocusing method in microwave imaging without background information, J. Korean Soc. Ind. Appl. Math., 27 (2023), 109–122.
[52] S.-H. Son, N. Simonov, H.-J. Kim, J.-M. Lee, and S.-I. Jeon, Preclinical prototype development of a microwave tomography system for breast cancer detection, ETRI J., 32 (2010), 901–910.
[53] M. Vogelius and D. Volkov, Asymptotic formulas for perturbations in the electromagnetic fields due to the presence of inhomogeneities of small diameter, ESAIM: M2AN, 34 (2000), 723–748.
[54] T. Wick, Modified Newton methods for solving fully monolithic phase-field quasi-static brittle fracture propagation, Comput. Meth. Appl. Mech. Eng., 325 (2017), 577–611.